Accepted Manuscript

Nuclear blebbing of biologically active organoselenium compound towards human cervical cancer cell (HeLa): *In vitro* DNA/HSA binding, cleavage and cell imaging studies

Masood Ahmad Rizvi , Mehvash Zaki , Mohd. Afzal , Manoj Mane , Manjeet Kumar , Bhahwal Ali Shah , Saurabh Srivastav , Saripella Srikrishna , Ghulam Mustafa Peerzada , Sartaj Tabassum

Please cite this article as: M.A. Rizvi, M. Zaki, M. Afzal, M. Mane, M. Kumar, B.A. Shah, S. Srivastav, S. Srikrishna, G.M. Peerzada, S. Tabassum, Nuclear blebbing of biologically active organoselenium compound towards human cervical cancer cell (HeLa): *In vitro* DNA/HSA binding, cleavage and cell imaging studies, *European Journal of Medicinal Chemistry* (2015), doi: 10.1016/j.ejmech.2014.12.014.

Graphical abstract

Complex 1

Nuclear blebbing of biologically active organoselenium compound towards human cervical cancer cell (HeLa): *In vitro* DNA/HSA binding, cleavage and cell imaging studies

Masood Ahmad Rizvi,[†] Mehvash Zaki,[‡] Mohd. Afzal,[‡] Manoj Mane,[§] Manjeet Kumar,[‖] Bhahwal Ali Shah,[‖] Saurabh Srivastav,[⊥] Saripella Srikrishna,[⊥] Ghulam Mustafa Peerzada[†] and Sartaj Tabassum[‡]*

[†]*Department of Chemistry, University of Kashmir, Hazratbal, Srinagar–190006, J&K India.*
[‡]Department of Chemistry, Aligarh Muslim University, Aligarh–202002, India
[§]*Centre for Material Characterization, CSIR National Chemical Laboratory (NCL) Pune India.*
[‖]*Natural Product Microbes, CSIR–Indian Institute of Integrative Medicine (IIIM), Jammu Tawi–180001, J&K, India.*
[⊥]*Department of Biochemistry, Faculty of Science, Banaras Hindu University, Varanasi 221005, India*
Corresponding author: Tel.: +91 9358255791
E–mail address: tsartaj62@yahoo.com (S. Tabassum)

ABSTRACT

New pharmacophore organoselenium compound (**1**) was designed, synthesized and characterized by various spectroscopic methods (IR, ESI–MS, ^{1}H, ^{13}C and ^{77}Se NMR) and further confirmed by X–ray crystallography. Compound **1** consists of two 3,5–bis(trifluoromethyl)phenyl units which are connected to the selenium atom *via* the organometallic C–Se bond. *In vitro* DNA binding studies of **1** was investigated by absorption and emission titration methods which revealed that **1** recognizes the minor groove of DNA in accordance with molecular docking studies with the DNA duplex. Gel electrophoretic assay demonstrates the ability of **1** to cleave pBR322 DNA through hydrolytic process which was further validated by T4 religation assay. To understand the drug–protein interaction of which ultimate molecular target was DNA, the affinity of **1** towards HSA was also investigated by the spectroscopic and molecular modeling techniques which showed hydrophobic interaction in the subdomain IIA of HSA. Furthermore, the intracellular localization of **1** was evidenced by cell imaging studies using HeLa cells.

Keywords: Organoselenium compound; X–ray crystallography; DFT studies; DNA binding; pBR322 hydrolytic cleavage; GPx activity.

Abbreviations

UV–vis   UV–visible

CT DNA   Calf thymus DNA

Tris   Tris(hydroxymethyl)aminomethane

EB   Ethidium bromide

1. Introduction

Medicinal inorganic chemistry is an interdisciplinary thrust area of chemical research; is currently much more known for its many applications in catalysis and also has enormous potential to act as therapeutic and diagnostic agents. There is a growing interest in the field of small molecules capable of binding to deoxyribonucleic acid (DNA) has received immense influence in the development of new therapeutic modalities for cancer chemotherapy owing to the fact that many present treatment regimes (Platinum based drugs) in chemotherapy have failed or fall short either in terms of efficiency or toxicity problems [1–3]. Therefore, other non–platinum complexes have been evaluated in cancer chemotherapy, and in particular organometallic compounds have been extensively investigated for their medicinal properties [4–6]. Koepf and Koepf–Maier started to explore the anticancer activity of titanocene dichloride, in the 1970s with several clinical trials conducted (trials on actual patients with various forms of cancer that have not responded to existing treatments, including surgery, chemotherapy, and radiotherapy), although finally the compound was not approved for use [7]. Nevertheless, the early and highly promising research on $Ti(\eta_5–C_5H_5)_2Cl_2$ inspired other researchers to study the anticancer properties of organometallic compounds, who brought rational design and many new

2

ideas for the development of cancer chemotherapeutic drugs. Among the non–platinum complexes for metal based chemotherapy, organometallic selenium (Se)–containing molecules are emerging as new chemotherapeutic agents due to their ability to modulate multiple physiological effects on a wide range of cancer cell types as well as reverse the activity of drug resistance mechanisms to potentiate chemotherapy/radiotherapy efficacy [8]. The trace element selenium (Se), at very high doses is potential toxic and fatal for the human body, but the low doses of Se supplementation (nutritional intake of 50–350 μg per day) is seems to be beneficial not only for cancer prevention, but also influence other functions in organism by reducing inflammations, heart diseases and regulating the blood pressure. Moreover, selenium is essential for cell metabolism as a constituent of several seleno–proteins, including glutathione peroxidase, thioredoxin reductase etc which are primarily involved in antioxidant functions and maintenance of redox state [9]. Since the discovery of the first GPx (Glutathione Peroxidase) mimics organoselenium compound, 2–phenyl–1,2–benzoisoselenazol–3–(2H)–one (ebselen), considerable efforts have been made for the design and development of several organoselenium compounds as GPx mimics for the treatment of oxidative stress initiated by excess reactive oxygen species (ROS), and thereby preventing the cellular damage [10].

DNA is the essential carrier of genetic information which is concerned with most cancers resulting from DNA damage, and thus it is considered as a main target for anticancer drugs development. Interaction between small molecules and DNA is of great significance in the elucidation of the mechanisms of anticancer drugs and the screening of DNA targeted drugs [11].

In view of the aforementioned fact, the present work embodies the spectroscopic and single crystal X–ray diffraction of the newly synthesized bis(3,5–bis(trifluoromethyl)phenyl)selane. It would be pertinent to mention here that synthesis of

compound **1** was based on our understanding of a series of diselenides synthesized by our group, wherein we found that the molecule having bistrifluoromethyl phenyl moiety displayed most potent anticancer activity [12]. With this rationale, *in vitro* DNA binding profile of organoselenium compound **1** with CT–DNA and cleavage studies of **1** with pBR322 plasmid DNA by agarose gel electrophoresis was evaluated. The role of organoselenium compound **1** was not only merely antioxidative (by detoxification of reactive oxygen species as part of glutathione peroxidases), but rather acting as a DNA binding and cleaving agent. Furthermore, affinity of **1** towards human serum albumin (HSA) was also investigated since the drug–albumin interaction plays an important role in drug distribution and pharmacokinetics which influences the solubility of the prospective drug, extend its *in vivo* half–life, slow down or prevent its passive extravasations to the target tissues [13]. These studies provide an important rationale for the design of new lead anticancer drugs and their specific delivery at the active site of action, besides providing the pharmacological profile *in vitro*.

2. Results and Discussion

We report the synthesis of new organoselenium bis(3,5–bis(triflouromethyl)phenyl)selane compound **1** and the detailed procedure was described in experimental section (Scheme I) [14]. The product was isolated as a yellowish red solid, and suitable crystals for X–ray diffraction analysis was grown by slow evaporation of its solution in CHCl₃/MeOH (8:2 v/v), over a period of one week at room temperature. The resulting compound **1** was stable towards air and moisture and readily soluble in DMSO and MeOH. The single–crystal X–ray analysis reveals that the compound **1** crystallizes in a triclinic crystal system with *P*–1 space group. The unit cell parameters were found to be $a = 8.7402(5)$ Å, $b = 8.9544(5)$ Å, $c = 12.4403(6)$ Å, $\alpha = 107.674(4)°$, $\beta = 102.497(4)°$, $\gamma = 99.079(5)°$ with unit cell volume, $V = 879.16(9)$ Å³. A

perspective view of the ORTEP diagram and molecular structure of compound **1** was shown in Figure 1. From the crystal structure it has been observed that two 3,5–bis(trifluoromethyl)phenyl moieties are attached to the Selenium atom. The C–Se–C bond angle is 100.9(2)°, as expected for the divalent sp^3 Se atom with lone pair–lone pair repulsions. Selected crystallographic data for the compound were summarized in Table S1. The crystal packing of compound **1** displayed the common feature of layers of weakly interacting stacked phenyl groups of one molecule with the other. Besides, 3D supramolecular architecture of compound **1** was generated which shows two types of secondary interactions, hydrogen and weak halogen bonding between the identical moieties of the same molecules (Figure 2). The distance between the hydrogen atoms of one molecule with the fluorine atom of another molecule is 2.658(2) Å (H–F), and fall in the range of moderate hydrogen bonding distance. Interestingly, the halogen (F–F) distance in compound **1** was 2.713(3) Å, which was quite favorable for halogen interactions thereby helping the molecules to interact and stay closer. Density functional theory (DFT) is a popular computational method of medicinal chemists widely used today for screening of biologically relevant molecular systems in a time and cost effective manner [15, 16]. The DFT studies were performed using Turbomole 6.0 program with B3LYP functional and three different basis sets {6-31G(d,P), LanL2MB, TZVP} for a close agreement of the optimized structure with the experimental crystal structure. To have an idea about ionization potential, electron affinity and any potential optical properties of the newly reported molecule the HOMO LUMO energies were also computationally worked out. The most appropriate match of optimized structure with the crystal structure was achieved at the B3LYP/TZVP level of theory in accordance with findings of Taubert et al [17]. In order to improve our calculations for HOMO and LUMO energies at a reasonably lower computational cost, we performed single point energy calculation of

B3LYP/TZVP optimized structure of compound **1** with larger TZVPP basis set [18]. Comparison of selected geometrical parameters of the X–ray crystallographic structure and DFT optimized structure of the bis(3,5–bis(triflouromethyl)phenyl)selane was depicted in Table 1. A high band gap of 4.6 eV, predicted that the compound was stable with respect to electron transfer. The electron density plots and molecular surfaces of HOMO and LUMO (Figure 3), indicated that the electron density in case of HOMO is concentrated on selenium metal and in case of LUMO the electron density is predominantly on the phenyl rings. Thus electron rich selenium atom of compound **1** has a nucleophillic character which also supports the proposed pathway of its DNA cleavage (see the Supporting Information Figures S1 and S2 and Scheme II).

In order to assess the possible pharmacological properties of compound **1**, a toxicity profile evaluation was performed by employing the OSIRIS software (http://www.organic–chemistry.org/prog/peo/). As depicted in Table 2, compound **1** does not show any toxicity risk that is non–mutagenic, non–tumorigenic, non–irritant and no reproductive effect. The log P (4.85) value was under the acceptable criteria (log P<5) indicating that the compound was quite hydrophilic in nature. Compound **1** also shows moderate to good drug likeness (–27.9) and drug score (0.17) which revealed that it could be considered as a drug candidate for oral absorption (Figure S3, Supporting Information).

2.1. DNA binding studies

DNA binding is very important in the development of new metal based chemotherapeutic agents. The electronic absorption spectrum of compound **1** in DMSO–buffer mixture exhibit an intense transition at 270 nm, attributed to the π–π* transition of the ligand. Upon increasing the concentration of CT DNA $(0–4.66) \times 10^{-5}$ M, a concomitant increase in absorption intensities was observed with hyperchromism of 31.1–75.2 % with red shift of 4 nm in the intraligand band

(Figure 4). The observed hyperchromic effect suggests that compound binds to DNA by external contact, and red shift was due to the participation of aromatic chromophores [19]. Since, DNA possesses several hydrogen bonding sites which are accessible both in major and minor grooves [20]. So it is likely that $-CF_3$ group present in the compound favor hydrogen bonding with the base pairs of DNA helix in the grooves. To compare quantitatively the binding affinity of compound, the intrinsic binding constant K_b was calculated by monitoring the changes in absorbance in the intraligand band at corresponding λ_{max} with increasing concentration of DNA. The K_b value of compound **1** was found to be $4.2 \times 10^4 \, M^{-1}$. The magnitude of DNA binding was greater for compound **1** than previously synthesized $Cu(II)-Sn(IV)_2$ heterobimetallic complex by our group ($3.0 \times 10^4 \, M^{-1}$).

Small molecules that bind and cleave at specific DNA sequences are widely used as fluorescent molecular probes for assessing the local structure of biomacromolecules such as nucleic acids and proteins [21]. Therefore, the binding ability of the small molecules with DNA was also investigated by fluorescence spectroscopic titration. Compound **1** emits intense luminescence when excited at 270 nm in 0.01 Tris–HCl/50mM NaCl buffer at room temperature with an emission maximum appearing at 361 nm. On addition of increasing amount of CT DNA, emission intensity of **1** decreases by 3.14 times than those in the absence of DNA and saturates at a ratio of [DNA]/[**1**] is 1.5, respectively (Figure 5). The quenching of emission intensity of **1** suggested the occurrence of molecule–molecule excitation interactions in the presence of DNA or changes in compound environment, such as hydrophobic interactions with the DNA binding sites *versus* hydrophilic interactions with the solvent molecules [22]. The binding constant (K) value for **1** was determined from Scatchard equation and found to be $2.07 \times 10^5 \, M^{-1}$. To further investigated the interaction of compound **1** with the DNA three–dimensional (3D) fluorescence

spectroscopy was performed on compound **1** in the absence and presence of CT–DNA (Figure S4, Supporting Information). The 3D fluorescence spectrum and contour ones of compound **1** consisted of two prominent peaks, peak A (λ_{ex} = 270 nm) and peak B (λ_{em} = 361 nm) showing the fluorescence behavior. However, upon addition of DNA, the fluorescence intensity of both the peaks excitation peak A and emission peak B decreases significantly indicating either partial intercalation or electron/energy transfer with double–stranded DNA which was in good agreement with that derived by absorption spectral and fluorescence measurements.

Competitive binding of drugs to DNA with EB could provide rich information with regard to the DNA binding affinity [23]. The EB fluorescence intensity will be enhanced in the presence of DNA because of its intercalation into the helix, and it is quenched by the addition of another molecule either by replacing the EB [24]. The extent of reduction of the emission intensity gives a measure of the binding propensity of the compounds to CT–DNA. The emission spectra of EB bound to DNA in the absence and presence of compound **1** was shown in Figure 6. Upon increasing concentration of the **1**, the emission band at 591 nm was quenched up to 44.71%, of the initial fluorescence intensity accompanied by red shift of 22 nm. The observed decrease in the fluorescence intensity with a strong red shift clearly indicates that the EB molecule was displaced by the **1** from their DNA binding sites [25]. Furthermore; the quenching extents was evaluated quantitatively by employing Stern–Volmer equation. The K_{sv} value for compound **1** was found to be 1.2 revealing that some of the EB was displaced from their DNA binding sites.

2.2. Fluorescence quenching studies with HSA

Human serum albumin is the most abundant plasma protein (~60% of total plasma protein) providing a depot and carrier for many endogenous and exogenous compounds with a crucial

effect on the drug distribution and pharmacokinetics [26]. The emission quenching experiment of HSA was carried out to study the interaction of compound **1** with HSA (Figure 7) [27]. The fluorescence spectra of HSA in the absence and presence of compound **1** as a quencher in Tris–HCl buffer (pH 7.4) was monitored with an excitation wavelength of 293 nm.

Upon the addition of increasing concentration of compound **1** (3.33×10^{-6} to 26.6×10^{-5} M) to fixed amount of HSA, significant decrease in the intrinsic fluorescence intensity of HSA was observed at 362 nm with a slight blue shift in the wavelength clearly indicating that the secondary structure of protein could be altered [28]. The observed blue shift was mainly attributed to the reduction in the polarity of the microenvironment around the Trp residues after the addition of **1** and the binding of **1** to the hydrophobic sites of HSA near the subdomain IIA [29].

In order to speculate the possible fluorescence quenching mechanism of HSA in presence of compound **1,** Stern–Volmer equation was applied:

$$\frac{F_o}{F} = 1 + K_q \tau_o [Q] = 1 + K_{sv}[Q] \qquad (7)$$

where F_o and F are the fluorescence intensities in the absence and presence of quencher, while K_q, is the biomolecular quenching rate constant of the biomolecules and so is the average life time of the molecule without quencher ($\tau_o = 10^{-8}$ s), K_{sv} is the Stern–Volmer quenching constant, and [Q] is the concentration of the quencher, respectively. The Stern–Volmer plots of F_o/F versus [Q] for the quenching of HSA fluorescence by compound **1** was depicted in Figure S5 (See Supporting Information) and the calculated K_{SV} and K_q value was found to be 7.63×10^3 M^{-1} and 7.63×10^{12} M^{-1}s^{-1}, respectively. The observed K_q value was larger than the limiting diffusion constant K_{dif} of the biomolecules ($K_{dif} = 2.0 \times 10^{10}$ M^{-1}s^{-1}), [30] indicating that the fluorescence quenching was caused due to the specific interaction of compound **1** with HSA, consistent with

9

the static quenching mechanism [31]. For static quenching, the Scatchard equation was employed to calculate the binding constant and number of binding sites [32]:

$$\log[\frac{F_o - F}{F}] = \log K + n \log[Q] \qquad (8)$$

where F_o and F are the fluorescence intensities of HSA in the absence and presence of quencher, K and n are the binding constant and the number of binding sites, respectively. Thus, a plot of $\log[(F_o–F)/F]$ versus $\log[Q]$ was used to determine K (binding constant) from the intercept on Y–axis and n (binding sites) from the slope (Figure S6, Supporting Information). From the corresponding Scatchard plot, the K values were found to be 0.416 for compound **1** while the n was calculated to be 1.46, respectively.

In order to further gain insight in the conformational changes of HSA, 3D fluorescence spectral studies was carried out in the presence and absence of compound **1**. The 3D fluorescence spectra and contour ones of HSA and compound **1**–HSA system were shown in Figure 8. Peak A was the Rayleigh scattering peak ($\lambda_{ex} = \lambda_{em}$). Peak B (295, 332 nm, λ_{ex}, λ_{em}) dominatingly displays spectral behavior of the Trp residue, and the fluorescence intensity of this residue was associated with its micro–environment′s polarity. The results revealed that fluorescence intensity of both peaks peak A and peak B (295, 332 nm, λ_{ex}, λ_{em}) decreases significantly indicating the quenching of fluorescence induced by Trp residue of HSA. However, the fluorescence intensity of peak B was strongly quenched revealing that **1** binds to HSA near the tryptophan residues [33]. These results revealed that the interaction of **1** with HSA induced micro–environmental changes in the structure of HSA, corroborated well with our spectroscopic results.

2.3. DNA cleavage activity

The ability of compounds to cleave supercoiled (SC) pBR322 DNA was assayed by gel electrophoresis in the absence and/or presence of external agents. If one strand is cleaved, the SC DNA produces a slower–moving nicked circular (NC) form. If both strands are cleaved, the linear (L) form is generated which migrates in between the SC and NC forms [34]. With increasing concentration of **1**, the amount of SC form decreases gradually and there was conversion to NC form with simultaneous increase in the intensity of the latter form. It was clearly observed that at 25 μM concentration, **1** was found to promote the cleavage of DNA from supercoiled form (SC) to nicked circular form (NC) (Figure S7, Supporting Information) revealing the single strand DNA cleavage. Quantification of the both the forms originating from SC and NC plasmids by using Vilber–INFINITY gel documentation system were depicted in Figure S7c and S7d (See Supporting Information).

To predict the cleavage mechanism of pBR322 plasmid DNA by compound **1**, reactions were carried out in the presence of hydroxyl radical scavengers (DMSO and EtOH), singlet oxygen scavenger (NaN$_3$) and superoxide dismutase (SOD) as superoxide ion radical ($O_2^{\bullet-}$) scavenger (Figure 9). The significant inhibition of cleavage in the presence of DMSO and EtOH was observed indicating that **1** cleaves DNA might be through hydrolytic pathway. The addition of NaN$_3$ (lane 6) decreases the strand scission implying that the singlet oxygen or a singlet oxygen–like entity may be also involved in the cleavage reaction. However, SOD did not show any effect on DNA cleavage which clearly rule out the participation of superoxide radical ($O_2^{\bullet-}$). The results revealed that the presence of electron rich organoselenium compound **1** provides an inbuilt nucleophile Se, which facilitates the nucleophilic attack towards the phosphorus, followed by the formation of five–coordinate phosphate intermediate and subsequent rearrangement of the phosphate allows the DNA to be cleaved readily (Scheme SI, Supporting Information). The

DNA groove binding propensity of the compound was also studied using compound **1**, DNA minor groove binder DAPI and major groove binger methyl green. The cleavage pattern demonstrated that the inhibition in the DNA cleavage activity was observed in the presence of DAPI revealing the minor groove binding.

To further confirm the hydrolytic pathway mediated by compound **1**, DNA religation experiment was performed in which supercoiled pBR322 DNA was treated with T4 ligase enzyme and subjected to gel electrophoresis. It is well known that in DNA hydrolytic cleavage, $3'$–OH and $5'$–OPO$_3$ ($5'$–OH and $3'$–phosphate) fragments must be exclusively afford and that these fragments can be enzymatically ligated [35]. In some cases, the hydrolytic products either did not end at the required $5'$–phosphate and $3'$–OH (ribose) termini or the compound sometimes bound to the termini of cleaved DNA. These reasons would result in the religation being incomplete or even failing completely [36]. Compound **1** yielded nicked DNA which was religated by using T4 DNA ligase enzyme. Under our experimental conditions, the nicked form (Form II) was religated to a large extent in the presence of T4 ligase enzyme which was quantitatively ascertained by comparison of compound treated DNA and control DNA alone in supercoiled form providing direct evidence in favor of hydrolytic mechanism (Figure 10). Moreover, addition of T4 ligase showed significant retardation in mobility of religated DNA relative to that of control supercoiled DNA as a relatively sharp band during electrophoresis. Change in the electrophoretic mobility of plasmid DNA might be due to the strong binding of DNA T4 ligase at the ligation site.

2.4. Glutathione Peroxidase Activity

Glutathione peroxidase (GPx) belongs to the family of selenoproteins and plays an important role in the defense mechanisms oxidative damage by catalyzing the reduction of a variety of

hydroperoxides, using glutathione as the reducing substrate. Therefore, much effort has been made to mimic the function of GPx activity using small organoselenium molecules as a scaffold in which the catalytic selenium is introduced for therapeutic applications. The catalytic site of GPx enzyme includes a selenocysteine residue in which the selenium undergoes a redox cycle involving the selenol as the active form that catalyzes the reduction of harmful peroxides in the presence of cofactor glutathione (GSH) and thereby protects the lipid membranes as well as biologically important molecules against oxidative stress [37, 38]. The enzyme–catalyzed reduction of peroxide by GSH was studied according to the method reported by Tomoda et al by using organoselenium compound **1** as a GPx mimic [39]. In this assay, the catalytic GPx model reaction was initiated by the addition of an excess amount of H_2O_2 to a solution of GSH containing a selenium catalyst and was monitored by UV spectroscopy at 305 nm. The initial reduction rates of H_2O_2 (v_0) were obtained by monitoring the increase in UV absorption at 305 nm due to the formation of corresponding disulfide (GSSG). However, the reduction rate of H_2O_2 without any compound was very slow (1.21 mM min^{-1}) but a considerable enhancement in the Gpx activity was observed on increasing the concentration of organoselenium compound **1** (14.2 mM min^{-1}) revealing that **1** act as excellent GPx mimic (Figure 11). Therefore, the synthetic organoselenium compound involves the rapid cleavage of the aliphatic carbon– selenium bond when employed as catalysts for the reduction of hydroperoxides. The 3,5– bis(trifluoromethyl)benzene was used as cofactors and the catalytic mechanism involves the formation of different intermediates which was responsible for the reduction of hydrogen peroxide with GSH (Scheme II).

2.5. Docking studies with DNA and HSA

13

To ascertained the groove binding mode of compound **1** obtained from gel electrophoretic results, compound **1** was docked on DNA duplex of sequence d(CGCGAATTCGCG)$_2$ dodecamer (PDB ID: 1BNA). The resulting model showed that compound **1** recognizes DNA in the minor groove situated within G–C rich region from chain A (G2A and C3A) through aromatic benzene ring and stabilized by van der Waal′s interactions and hydrophobic contacts with DNA functional groups. Moreover, fluorine atoms of the compound **1** may be engaging in hydrogen–bonding interactions with DNA nucleobases DG14 (3.55, 2.71 Å), DG16 (2.51, 3.00 Å) and DG10 (2.46, 3.55 Å) available in the minor grooves in GC rich sequences (Figure 12). The resulting relative binding energy of docked metal compounds **1** DNA was found to be –3.77 Kcal/mol, indicated that compound **1** strongly binds to the DNA, which is correlated well with the experimental DNA binding results.

Similarly, the quenching of Trp214 residues in presence of compound **1** was also validated by molecular docking technique. HSA comprises three homologous domains (denoted I, II, and III): I (residues 1–195) II (196–383) and III (384–585); each domain has two subdomains (A and B) that assemble to form heart shaped molecule. The principal region of drug binding sites of HSA are located in hydrophobic cavities in subdomain IIA and IIIA, corresponding to site I and site II, respectively and tryptophan residue (Trp–214) of HSA in subdomain IIA [40, 41]. The model revealed that the compound **1** was inserted in the hydrophobic cavity of site I, and was close proximity to the tryptophan residue of HSA (Trp214), suggesting the existence of hydrophobic interaction between them. Such finding provides a good structural basis to explain the very efficient fluorescence quenching of HSA emission in the presence of compound **1**. At the same time, there were considerable number of hydrogen bonds and electrostatic interactions between Arg–160 and Arg–257 and Ala–291 and fluorine atoms of

compound **1**. On the other hand, the amino acid residues with aromatic ring could match with that of the benzene ring of compound **1** and stabilized by π–π staking interaction in space to firm the binding environment of the compound **1** (Figure 13 and Figure S8, Supporting Information).

2.6. Docking studies with Glutathione peroxidase

To gain insights into the biological effects of organoselenium compound serve as Glutathione peroxidase mimics, compound **1** was successively docked with the target enzyme to understand the interaction of compound **1** with the target active–site. The active sites of GSH peroxidase are found in flat depressions on the molecular surface and are readily accessible from solvent channels in the crystals. The catalytic triad of GPXs is composed of the selenocysteine, a glutamine and tryptophan amino acid residues [42]. Exposure of the catalytically active selenocysteine residues at the molecular surface is consistent with the easy access of the substrates and thus the high reaction rates of GSH peroxidase [43]. The resulting docked model clearly indicated that some aromatic amino acid residues Ala138, Cys152, Ser157, Arg153, Met140, Thr137, Asn114, Asn154, Asp155 and Trp148 are found in the close proximity with that of compound **1** showing the electrostatic interactions in the active site (Figure 14). The amino acid residues Pro143, Ile146, Val151 of GPx and was involved in the van der Waal interactions with compound **1**. Similarly, the selenium atom was involved in van der Waal interactions with Leu139 amino acid residues. Furthermore, hydrogen bonding of Tryp148, Asn154 and Asp155 residues at the active site with the fluorine atom of the compound **1** enhances the reactivity of Se towards hydroperoxides [44]. The total interaction energy was found to be –10.39 kcal/mol, indicating that the non–covalent interactions are important criteria for the catalytic reduction of hydrogen peroxide and organic peroxides. The results suggested that high GPx activity of compound **1** was due to the presence of hydrogen bonding, electrostatic

and van der Waal interactions within the active site of GPx catalytic triad. Therefore, compound **1** was acting as a GPx mimic, which effectively scavenged hydroperoxides and protected the mitochondria against oxidative damage.

2.7. Cell imaging studies

The anticancer activity of organoselenium compound **1** was investigated against HeLa cell line by using the MTT assay and confocal microscopy for cell viability and cell imaging studies respectively for documenting intracellular changes due to apoptosis. The HeLa cells were incubated with an increasing concentration of **1** separately for 24 h. The results revealed concentration–dependent decline in the number of viable HeLa cells. It was found that at 30 μM concentration cell viability was reduced to around 68 percent. While, at 40 μM concentration cell viability was reduced to less than 50 percent. Increasing concentration further resulted in progressive decrement in cell viability as shown in Figure S9 (See Supporting Information).

To gain further insight in the mechanism of cell death, confocal microscopy was performed as a preliminary investigation of its applicability as an anticancer therapeutics. The control and treated cells were stained with PI (Propidium Iodide), a nucleus specific dye that helps in understanding nuclear morphology. Cell imaging of Propidium Iodide stained cell that were already treated with compound **1** revealed nuclear condensation with blebbing and fragmentation of nuclei, which was typical of late apoptosis (inset in Figure 15 c). However, no such blebbing was observed in control (inset in Figure 15 f). Therefore, the potential compound **1** to initiate nuclear blebbing in HeLa cancer cell line suggests its efficacy for utilizing it in anti–cancer chemotherapeutics.

3. Experimental

3.1. Reagents and Materials

All reagents were commercially available and used as supplied without further purification. 6X loading dye (Fermental Life Science) and Supercoiled plasmid DNA pBR322 (Genei) were utilized as received.

HSA (fatty acid free, 99%) was purchased from Sigma and used without further purification. Human serum albumin of 1×10^{-3} M was prepared by dissolving protein in Tris–HCl buffer solution at pH 7.3. The protein concentration was determined spectrophotometrically using an extinction coefficient of 35219 M^{-1} cm^{-1} at 280 nm. NaCl (analytical grade, 1 M) solution was used to maintain the ionic strength of buffer at 0.1 M, pH was adjusted to 7.3 by using HCl. Working standard solution was obtained by appropriate dilution of the stock solution.

3.2. Methods and instrumentation

The Crystal structure was solved using Super Nova Dual source X-ray Diffractometer system (Agilent Technologies) equipped with a CCD area detector and operated at 250 W power (50 kV, 0.8 mA) to generate Mo Kα radiation (λ = 0.71073 Å) and Cu Kα radiation (λ = 1.54178 Å) at 293(2) K. ^{1}H and ^{13}C NMR spectra were recorded on Bruker–Avance DPX FT–NMR 400 MHz spectrometer with TMS as an internal standard. The IR spectra were recorded as KBr pellets with Shimadzu IR–408 Perkin–Elmer 1800 (FTIR) and its values are given in cm^{-1}. Chemical shifts are expressed in parts per million (δ ppm). HRESIMS were recorded on G6540–UHD LC/MS Q–TOF Agilent Technologies. Silica gel coated aluminum plates were used for TLC. All the reagents used were of analytical grade. Electronic spectrum was recorded on UV–1700 PharmaSpec UV–vis spectrophotometer (Shimadzu) in DMSO cuvettes of 1 cm path length. Data were reported in λ_{max}/nm. Fluorescence measurements were determined on a RF–5301 PC spectrofluorophotometer (Schimadzu). DNA cleavage experiments were performed with the help

17

of Axygen made electrophoresis supported by a Genie power supply with a potential range of 50–500 volts, visualized and photographed by a Vilber–INFINITY gel documentation system.

3.3. Synthesis of Bis(3,5–bis(triflouromethyl)phenyl)selane (1). Selenium powder (1.98 g, 25.0 mmol) was stirred for 15 min in dry THF, in a two necked 50 ml round bottomed flask, followed by addition of distilled SO_2Cl_2 (2.00 g, 28.0 mmol) at 0 °C. The mixture was kept on stirring for another 1 h to obtain a clear brownish red solution of $SeCl_2$. In another two necked 100 ml round bottomed flask freshly activated Mg turnings were vigorously stirred in THF for 5 min, followed by addition of 1–bromo–3,5–bis(trifluoromethyl)benzene (7.28 g, 25 mmol) and kept on stirring for 6 h. After formation of Grignard reagent, $SeCl_2$ (0.5 eqiv.) solution was added drop wise *via* cannulation at –78 °C and allowed to warm to room temperature. The progress of the reaction was monitored by thin layer chromatography. After completion, the mixture was poured into water and extracted with ethyl acetate (3 × 50 ml). The combined organic layers were dried over sodium sulfate and solvents were removed under vaccum through rotary evaporator. The crude extract was purified by column chromatography using hexane:ethyl acetate (5:1) to afford pure bis(3,5–bis(triflouromethyl)phenyl)selane as a yellowish red solid in 85% yield (10.73g). ^{1}H NMR (400 MHz, CDCl$_3$): δ 7.78 (s, 4H), 7.92 (s, 2H). ^{13}C NMR (100 MHz, CDCl$_3$): δ 121.6, 122.3, 123.7, 131.5, 132.1, 132.3, 132.6, 132.8. ^{77}Se NMR: δ 485.185. HRESI–MS found for $C_{16}H_6F_{12}Se$ [M+H]$^+$: 506.1634 (calcd. $C_{16}H_6F_{12}Se$ [M+H]$^+$: 506.1671) {See Supporting Information Figures S10–S13}.

3.4. Computational Details

3.4.1. DFT studies

The DFT calculations were performed using TURBOMOLE 6.0 computational chemistry program [45]. The geometry optimization of the Bis(3,5–bis(triflouromethyl)phenyl)selane was carried out with B3LYP functional [46] which has a proven track record of predicting the

structures and the energetics accurately [47]. Three basis sets 6–31G(d,p) [48], LanL2MB [49] and TZVP [50] were examined for the perfect matching of the optimized structure of compound 1 to its crystal structure [51]. The single point energy calculation of the B3LYP/ TZVP optimized structure was attempted using TZVPP basis set [52].

3.4.2. Molecular docking studies

The molecular docking studies were performed using Argus lab software, [53–55] an interactive molecular graphics program for calculating and displaying feasible docking modes of pairs of protein, enzymes and DNA molecule. Minimization was performed by geometry convergence function of ArgusLab software according to Hartree–Fock calculation method. Semi–emperical PM3 method was used for the geometrical optimization of ligand and charm force field was used for the preparation of receptor after that we have performed docking in which ligand is used as a flexible mode. The crystal structure of the B–DNA dodecamer d(CGCGAATTCGCG)$_2$ (PDB ID: 1BNA), human serum albumin (PDB ID: 1h9z) and glutathione peroxidase (PDB ID: 1GP1) were downloaded from the protein data bank. Visualization of the docked file has been done using Discovery studio molecular graphics programs.

3.5. DNA Binding and cleavage Experiments

DNA binding experiments include absorption spectral traces and emission spectroscopy conformed to the standard methods and practices previously reported in literature, [56–58] whereas DNA cleavage experiment has been performed by the standard protocol [59]. While measuring the absorption spectra an equal amount of DNA was added to both the compound solution and the reference solution to eliminate the absorbance of the CT DNA itself, and Tris buffer was subtracted through base line correction.

3.6. Fluorescence quenching studies with HSA

Fluorescence quenching measurements were carried out at excitation and emission wavelengths set at 293 and 200–800 nm, respectively. The interaction of compound **1** (0.67×10^{-5} to 4.6×10^{-5} M) with the HSA content of fixed concentration (6.67×10^{-6} M) was studied. The intensity at 362 nm (Trp–214) was used to calculate the binding constant (K) and 3D fluorescence spectra of HSA (1.5 mM) in the absence and presence of compound **1** (11.5 mM) were recorded in Tris–HCl buffer (pH 7.3) at room temperature by using Hitachi F–2700 fluorescence spectrophotometer.

3.7. Glutathione Peroxidase Assay

The GPx activity of the organoselenium compound **1** was determined through a spectrophotometric method at 305 nm. The test mixture contained GSH (2 mM), EDTA (20 mM), glutathione reductase (2.5 U/mL), and NADPH (2 mM) in 0.05 M potassium phosphate buffer, pH 7.0. The GPx samples (30 μl–0.3 ml) were added to the test mixture at 25 °C, and the reaction was started through the addition of H_2O_2 (2.5 mM). The initial reduction rates were calculated from the oxidation rate of NADPH. The initial reduction rate was determined at least three times and calculated from the first 5–10% of the reaction using 6220 $M^{-1}cm^{-1}$ as the extinction coefficient for NADPH.

3.9. In–vivo study of Bis(3,5–bis(triflouromethyl)phenyl)selane (**1**)

The efficacy of compound **1** as an anti–cancerous chemotherapeutics in live cell was undertaken in HeLa cell line.

3.10. Maintenance of cell lines

HeLa cell line was maintained in DMEM (Dulbeco's Modified Eagle Medium) medium supplemented with 10% FBS (Fetal Bovine Serum) and 1% antibiotics and antimycotic (Himedia) as per manufacturer's protocol. Cells were incubated in CO_2 incubator at 5% CO_2 and 37 ^{o}C temperature.

3.11. Cell Proliferation and viability assay

To measure cell viability and growth MTT assay was done. In this assay, cells seeded in 96–well plates ($5x10^3$cells/ well) in duplicate were cultured in complete DMEM medium. Cells were treated with different concentrations of compound **1** (10, 20, 30, 40, 50 µM) separately for 24 hours. The cells, after treatment were incubated with MTT for 2 hours. The yellow tetrazolium salt (MTT) is reduced in metabolically active cells to form insoluble purple formazan crystals, which are solubilised by the addition of DMSO (Sigma). The colour was then quantified by spectrophotometric measurement at 570 nm wavelength on a microtiter plate reader (Bio–Rad model 680 microplate reader).

3.12. Confocal imaging of compound 1 treated HeLa cells

We proceeded for utilization of "compound **1**" as an anti–cancerous chemotherapeutics in HeLa cell line treated with "compound **1**". In this study HeLa cells were incubated separately with 30 µM of compound **1** for 60 min in dark. Cells were washed for 5min with 1X PBS (Phosphate buffered saline, pH 7.4) twice. Cells were stained with 1µg/ml concentration of Propidium Iodide (PI) for 5 min in dark. Cells were washed for 5min with 1X PBS (Phosphate buffered saline, pH 7.4) twice. Cells collections after each step was done by centrifugation at 2000 rpm for 2min. Cells were mounted with DABCO on slide. Control for compound **1** was also taken. Slides were observed under 63X oil objective lens of Zeiss, LSM 510 Meta Confocal microscope.

21

4. Conclusion

The new organoselenium compound **1** was synthesized and thoroughly characterized by spectroscopic (IR, ^{1}H, ^{13}C, ^{77}Se NMR, HRESI–MS), analytical techniques and further validated by X–ray crystallography. The DFT study of **1** was also performed by using Turbomole computational chemistry program (B3LYP/TZVP method) and the HOMO–LUMO gap of 4.6 eV indicated the stability of molecule. *In vitro* DNA binding profile of compound **1** was carried out by using various biophysical techniques in accordance with molecular docking studies which revealed that **1** binds to DNA through external contact and hydrogen bonding, in addition to selective recognition towards the minor groove of DNA. Compound **1** cleaves supercoiled plasmid pBR322 DNA *via* hydrolytic cleavage mechanism induced by the nucleophilic Se atom which was further supported by DNA relegation assay by employing T4 DNA ligase. Furthermore, affinity of **1** towards HSA was also investigated by fluorescence spectroscopy to understand the carrier role of serum albumin for **1** in blood under physiological conditions. The antitumor activity of **1** was investigated by using MTT assay and confocal cell imaging studies which showed nuclear condensation and blebbing inside the HeLa cells typical of late apoptosis or necrosis. Therefore, compound **1** act as a promising candidate for GPx mimic and its potential to initiate nuclear blebbing in HeLa cancer cell line warrants further *in vivo* investigation.

Notes and References

Department of Chemistry, Aligarh Muslim University, Aligarh, UP–202202, India. Tel.: +91 9358255791: *E-mail address:* tsartaj62@yahoo.com

† Electronic supplementary information (ESI) available: Tables, and a CIF file and crystallographic data. Crystallographic data are also available from the CCDC as file CCDC 1023336. Crystallographic data for the structural analyses have been deposited with the Cambridge Crystallographic Data Centre, CCDC Copies of this information may be obtained free of charge from: The Director, CCDC, 12 Union Road, Cambridge CB2 1EZ, UK [fax: (int. code) +44 1223–336–033; e–mail: deposit@ccdc.cam.ac.uk or www: http://www.ccdc.cam.ac.uk]. Details of DFT studies, *in vitro* screening, DNA and HSA binding, concentration dependent DNA cleavage and mechanism for the hydrolytic cleavage.

References

[1] M. Alagesan, N. S. P. Bhuvanesh, N. Dharmaraj, Dalton Trans. 42 (2013) 7210–7223.

[2] S. H. van Rijt, P.J. Sadler, Drug Discov. Today 14 (2009) 1089–1097.

[3] (a) E. Ramachandran, D.S. Raja, J.L. Mike, T.R. Wagner, M. Zeller, K. Natarajan, RSC Advances 2 (2012) 8515–8525. (b) B.–d. Wang, Z.–Y. Yang, P. Crewdson, D.–q. Wang, J. Inorg. Biochem. 101 (2007) 1492–1504.

[4] G. Gasser, I. Ott, N. Metzler–Nolte, J. Med. Chem. 54 (2011) 3–25.

[5] B. Bertrand, A. Casini, Dalton Trans. 43 (2014) 4209–4219.

[6] Y.K. Yan, M. Melchart, A. Habtemariam, P.J. Sadler, Chem. Commun. (2005) 4764–4776.

[7] C.G. Hartinger, N.M. –Nolte, P.J. Dyson Organometallics 31 (2012) 5677–5685.

[8] M. Fakih, S. Cao, F.A. Durrani, Y.M. Rustum, Clinical Colorectal Cancer 5 (2005) 132–135.

[9] C.P. Prabhu, P.P. Phadnis, A.P. Wadawale, K.I. Priyadarsini, V.K. Jain, J. Organomet. Chem. 713 (2012) 42–50.

[10] Y. Nakamura, Q. Feng, T. Kumagai, K. Torikai, H. Ohigashi, T. Osawa, N. Noguchi, E. Niki, K. Uchida J. Biol. Chem., 277 (2002) 2687–2694.

[11] S. Liu, W. Cao, L. Yu, W. Zheng, L. Li, C. Fan, T. Chen, Dalton Trans. 42 (2013) 5932–5940.

[12] M.A. Rizvi, S. Guru, T. Naqvi, M. Kumar, N. Kumbhar, S. Akhoon, S. Banday, S.K. Singh, S. Bhushan, G.M. Peerzada, B.A. Shah, Bioorg. Med. Chem. Lett. 24 (2014) 3440–3446.

[13] B. Demoro, R.F.M. de Almeida, F. Marques, C.P. Matos, L. Otero, J.C. Pessoa, I. Santos, A. Rodriguez, V. Moreno, J. Lorenzo, D. Gambino, A.I. Tomaz, Dalton Trans. 42 (2013) 7131–7146.

[14] S.S. Zade, S. Panda, H.B. Singh, G. Wolmershauser, Tetrahedron Letters 46 (2005) 665–669.

[15] M. Sulpizi, G. Folkers, U. Rothlisberger, P. Carolini, L. Scapozza, Molecular Informatics, 21,(2002) 173–181.

[16] A. Lauria, R. Bonsignore, A. Terenzi, A. Spinello, F. Giannici, A. Longo, A.M. Almerico, G. Barone, Dalton Trans. 43 (2014) 6108–6119.

[17] S. Taubert, H. Konschin, D. Sundholm, Phys. Chem. Chem. Phys. 7 (2005) 2561–2569.

[18] M. Hermann, C. Goedecke, C. Jones, G. Frenking, Organometallics, 32 (2013) 6666–6673.

[19] E.S. Koumousi, M. Zampakou, C.P. Raptopoulou, V. Psycharis, C.M. Beavers, S.J. Teat, G. Psomas, T.C. Stamatatos, Inorg. Chem. 51 (2012) 7699–7710.

[20] R.A. Khan, A. Asim, R. Kakkar, D. Gupta, V. Bagchi, F. Arjmand, S. Tabassum, Organometallics 32 (2013) 2546–2551.

[21] A. Granzhan, H. Ihmels, Org. Lett. 7 (2005) 5119–5122.

[22] N. Shahabadi, M. Maghsudi, Mol. BioSyst. 10 (2014) 338–347.

[23] P. Krishnamoorthy, P. Sathyadevi, A.H. Cowley, R.R. Butorac, N. Dharmaraj, Eur. J. Med. Chem. 46 (2011) 3376–3387.

[24] S. Tabassum, M. Zaki, M. Afzal, F. Arjmand, Dalton Trans. 42 (2013) 10029–10041.

[25] X.–F. Zhao, Y. Ouyang, Y.–Z. Liu, Q.–J. Su, H. Tian, C.–Z. Xie, J.–Y. Xu, New J. Chem. 38 (2014) 955–965.

[26] J. Wu, P. Su, Y. Yang, J. Huang, Y. Wang, Y. Yang, J. Mater. Chem. B 2 (2014) 775–782.

[27] P. Krishnamoorthy, P. Sathyadevi, P.T. Muthiah, N. Dharmaraj, RSC Advances 2 (2012) 12190–12203.

[28] X.–F. Zhang, L. Xie, Y. Liu, J.–F. Xiang, L. Li, Y.–L. Tang, J. Mol. Struct. 888 (2008) 145–151.

[29] C.–H. Ng, W.–S. Wang, K.–V. Chong, Y.–F. Win, K.–E. Neo, H.–B. Lee, S.–L. San, R.N. Z.R.A. Rahman, W.–K. Leong, Dalton Trans. 42 (2013) 10233–10243.

[30] M. R. Eftink, Fluorescence Quenching Reaction: Probing Biological Macromolecular Structures, Biophysical and Biochemical Aspects of Fluorescence Spectroscopy, Plenum Press, New York, 1991.

[31] J.R. Lakowicz, G. Weber, Biochemistry 12 (1973) 4161–4170.

[32] U. Katrahalli, S. Jaldappagari, S. S. Kalanur, Spectrochim. Acta Part A 75 (2010) 314–319.

[33] J.–Q. Tong, F.–F. Tian, Q. Li, L.–L. Li, C. Xiang, Y. Liu, J. Dai, F.–L. Jiang, Photochem. Photobiol. Sci. 11 (2012) 1868–1879.

[34] S. Tabassum, M. Zaki, M. Afzal, F. Arjmand, Dalton Trans. 42 (2013) 10029–10041.

[35] M.E. Branum, A.K. Tipton, S. Zhu, L. Que, Jr, J. Am. Chem. Soc. 123 (2001) 1898–1904.

[36] M. Scarpellini, A. Neves, R. Horner, A.J. Bortoluzzi, B. Szpoganics, C. Zucco, R.A.N. Silva, V. Drago, A.S. Mangrich, W.A. Ortiz, W.A.C. Passos, M.C.B. de Oliveira, H. Terenzi, Inorg. Chem. 42 (2003) 8353–8365.

[37] G. Mugesh, H.B. Singh, Chem. Soc. Rev. 29 (2000) 347–357.

[38] E.E. Battin, N.R. Perron, J.L. Brumaghim, Inorg. Chem. 45 (2006) 499–501.

[39] M. Iwaoka, S. Tomoda, J. Am. Chem. Soc. 116 (1994) 2557–2561.

[40] J.H. Tang, F. Luan, X.G. Chen, Bioorg. Med. Chem. 14 (2006) 3210–3217.

[41] S. Tabassum, W.M. Al–Asbahy, M. Afzal, F. Arjmand, R.H. Khan, Mol. BioSyst. 8 (2012) 2424–2433.

[42] M. Birringer, S. Pilawa, L. Flohe, Nat. Prod. Rep. 19 (2002) 693–718.

[43] O. Epp, R. Ladenstein, A. Wendel, Eur. J. Biochem. 133 (1983) 51–69.

[44] B.K. Sarma, G. Mugesh, Org. Biomol. Chem., 6 (2008) 965–974.

[45] R. Ahlrichs, M. Bar, M. Haser, H. Horn, C. Kolmel, Chem. Phys. Lett. 162 (1989) 165–169.

[46] K. Kim, K.D. Jordan. J. Phys. Chem. 98 (1994) 10089–10094.

[47] P.E.M. Siegbahn, T. Borowski, Acc. Chem. Res. 39 (2006) 729–738.

[48] V.A. Rassolov, M.A. Ratner, J.A. Pople, P.C. Redfern, L.A. Curtiss, J. Comp. Chem. 22 (2001) 976–984.

[49] W. R. Wadt and P. J. Hay, J. Chem. Phys. 82 (1985) 284–298.

[50] S. Ansgar, H. Christian, A. Reinhart, J. Chem. Phys. 100 (1994) 5829–5835.

[51] J.K. Pearson, F. Ban, R.J. Boyd, J. Phys. Chem. A 109 (2005) 10373–10379.

[52] K. Eichkorn, O. Treutler, H. Ohm, M. Haser, R. Ahlrichs, Chem. Phys. Lett. 240 (1995) 283–290.

[53] J.J.P. Stewart, J. Comp. Chem. 10 (1989) 209–220.

[54] J.J.P. Stewart, J. Comp. Chem. 10 (1989) 221–264.

[55] M. Thompson, ArgusLab 4.0.1., Planaria software LLC, Seattle, Wash, USA, 2004.

[56] M.E. Reicmann, S.A. Rice, C.A. Thomas, P. Doty, J. Am. Chem. Soc. 76 (1954) 3047–3053.

[57] A. Wolfe, G. H. Shimer, T. Meehan, Biochemistry 26 (1987) 6392–6396.

[58] J.R. Lakowiez, G. Webber, Biochemistry 12 (1973) 4161–4170.

[59] F. Arjmand, M. Mudassir, R.H. Khan, Eur. J. Med. Chem. 45 (2010) 3549–3557.

Figure and Scheme Captions

27

Scheme I. Synthesis of bis(3,5–bis(trifluoromethyl)phenyl)selane.

Scheme II. Proposed mechanism for the Glutathione Peroxidase activity of compound **1**.

Fig. 1. ORTEP diagram of compound **1**.

Fig. 2. Molecular structure of compound **1** showing Ball and stick model.

Fig. 2. Diagramatic representation of 3D (a) view in wire frame model and (b) CPK model in compound **1**.

Fig. 3. Electrostatic potential map and HOMO–LUMO Energy separation of compound **1**.

Fig. 4. Absorption spectra of compound **1** in 5mM Tris HCl/ 50 mM NaCl buffer upon the addition of calf thymus DNA; Inset: Plots of [DNA]/ ε_a–ε_f (m^2 cm) vs [DNA] for the titration of CT DNA with compound **1** ▲, experimental data points; full lines, linear fitting of the data. [compound **1**] = $6.67{\times}10^{-6}$ M, [DNA] = $(0{-}4.66) \times 10^{-5}$ M. Arrow shows change in intensity with increasing concentration of DNA.

Fig. 5. Emission spectra of compound **1** in Tris–HCl buffer (pH 7.3) in the presence and absence of CT DNA at room temperature. Arrow shows change in intensity with increasing concentration of DNA.

Fig. 6. Emission quenching spectra of CT DNA bound ethidium bromide in the presence of (a) compound **1** in buffer 5 mM Tris–HCl/50 mM NaCl, pH = 7.3 at 25 ºC. Arrow shows change in intensity with increasing concentration of ethidium bromide.

Fig. 7. The fluorescence quenching spectra of HSA by different concentrations of compound **1** with the excitation wavelength at 293 nm in 5 mM Tris–HCl/50 mM NaCl buffer, pH 7.3, at room temperature: [HSA], 6.67×10^{-6} M; the concentration of compound **1** was

0.67×10⁻⁵ to 4.6×10⁻⁵ M. Arrow shows the intensity changes upon increasing concentration of the quencher.

Fig. 8. 3D fluorescence spectrum and corresponding contour diagrams of (a) HSA, and (b) compound **1**–HSA system. The concentration of HSA is fixed at 1.5 mM and that of compound **1** is fixed at 11.5 mM. pH = 7.3, at room temperature.

Fig. 9. Cleavage of pBR322 plasmid DNA (300ng) by **1** in 50 mM Tris–HCl/NaCl buffer (pH, 7.3) after incubation for 45 min in ptesence of (a) different scavenging and groove binding agents; Lane 1, DNA control; Lane 2, DNA + **1** + DMSO (0.4 mM); Lane 3, DNA + **1** + EtOH (0.4 mM); Lane 4, DNA + **1** + NaN$_3$ (0.4 mM); Lane 5, DNA + **1** + SOD (0.25 mM); Lane 6, DNA + **1** + DAPI (8 μM); Lane 7, DNA + **1** + MG (2.5 μL of a 0.01 mg/ml solution); (b) Quantification of band area in gel electrophoresis originating from Form I, Form II and Form III pBR322 plasmid DNA by **1** in the presence of various radical scavengers and groove binding agents. 2D projection of gel images for the cleavage of pBR322 plasmid DNA by **1** in presence of different radical scavengers (c) Form I bands, (d) Form II bands and (e) Form III bands.

Fig. 10. Agarose Gel electrophoresis for the (a) ligation pBR322 plasmid DNA linearised by compound **1**. Lane 1, DNA control; Lane 2, pBR322 plasmid DNA cleaved by compound **1**; Lane 3, ligation of nicked pBR322 plasmid DNA by T4 DNA ligase in presence of **1**. (b) Quantification of band area in gel electrophoresis originating from Form I and Form II pBR322 plasmid DNA by compound **1**. 2D projection of gel images for the cleavage of pBR322 plasmid DNA by compound **1** in presence and absence of T4 DNA ligase (c) Form I bands and (d) Form II bands.

Fig. 11. (a) Electronic absorption spectra in the presence of GPx mimic compound **1**. Arrow shows the changes in intensity at different time intervals. (b) Scavenging effects on the hydrogen peroxide upon increasing concentration of compound **1** (30 μl–0.4 ml), as determined through the Glutathione Peroxidase assay.

Fig. 12. Molecular docked model of compound **1** with DNA [dodecamer duplex of sequence d(CGCGAATTCGCG)₂ (PDB ID: 1BNA)]. (Relative negative binding energy; −3.77 Kcal/mol).

Fig. 13. Molecular docked model of (a) compound **1** (stick representation) located within the hydrophobic pocket in subdomain IIA of HSA. (b) The interaction mode between compound **1** (showing stick representation) and HSA (cartoon form).

Fig. 14. Molecular Docked model of (a) compound **1** (stick representation) located within the active site of glutathione peroxidase (PDB ID: 1GP1). (b) 2D diagram showing the binding site residues around compound **1** in the active site.

Fig. 15. Confocal images showing compound **1** treated (a, b, c) and control (d, e, f) HeLa cells. Cells nuclei were counter stained with Propidium Iodide (shown in red). DIC images of HeLa cell are shown in panels a, d and PI stained nuclei were shown in b, e while c, f are corresponding merge images. Note that arrow head in inset c shows clear nuclear blebbing in compound **1** treated HeLa cells while arrows in inset f point towards intact nuclei in untreated control cells. Images were taken under 63x oil objective lens of LSM 510 Meta confocal microscope, Zeiss.

Table 1: Selected Geometrical Parameters (Bond Lengths in Å, Bond Angles in deg) for the Bis(3,5–bis(triflouromethyl)phenyl)selane.

†Geometrical parameter	experimental	Theor. computed using B3LYP functional		
		TZVP	LanL2MB	6–31G
3C—S e	1.917	1.93	1.936	1.942
19 C—Se	1.93	1.93	1.933	1.942
24C—C 29	1.51	1.51	1.50	1.49
25H—F 35	2.445	2.89	2.49	2.48
C3—Se—C19	100.92	100.413	99.531	96.71
C2—C 3—S e	122.41	121.854	120.42	119.45
C29—C 24—C 26	119.61	120.724	120.63	119.60
C20—C 19—Se—C 3[a]	42.26	49.277	47.59	48.34

[a] Dihedral angle. †Atom labeling is based on Fig S1

Table 2: Osiris calculations of compound **1** showing the toxicity risk profile and molecular properties.

Compound	Toxicity risks				Molecular properties				
	MUT	TUM	IRRI	REP	MW	cLogP	S	D–L	D–S
1	🟩	🟩	🟩	🟩	506.0	4.85	–6.66	–27.9	0.17

MUT = Mutagenic, TUM = Tumorigenic, IRRI = Irritant, REP = Reproductive effective

Figure 1a

Figure 2
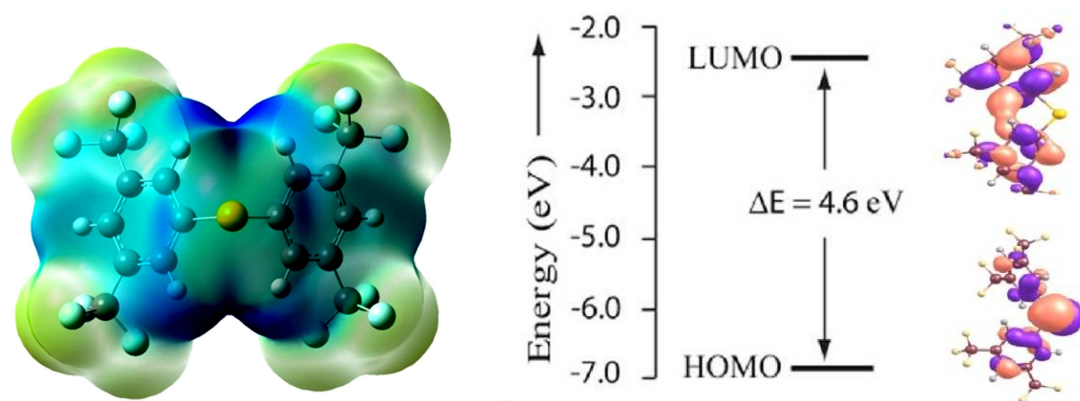
Figure 3
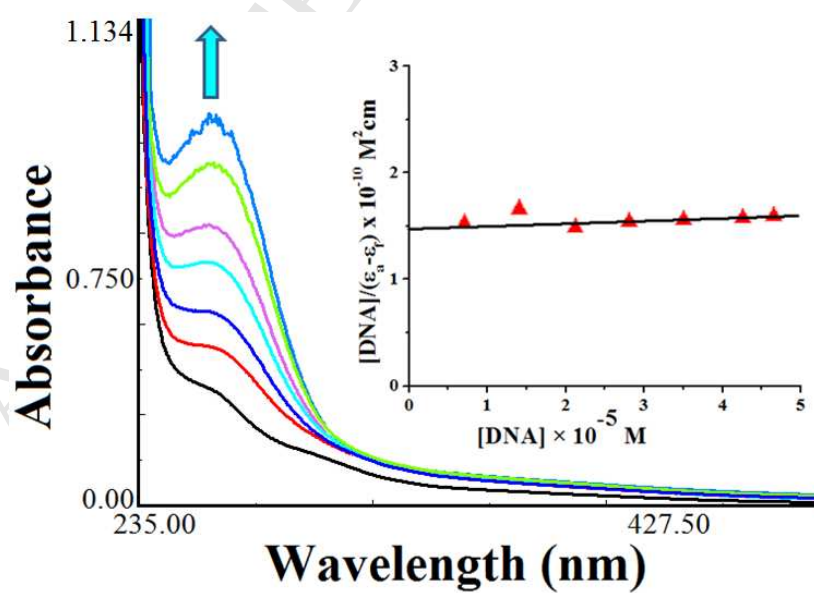
Figure 4
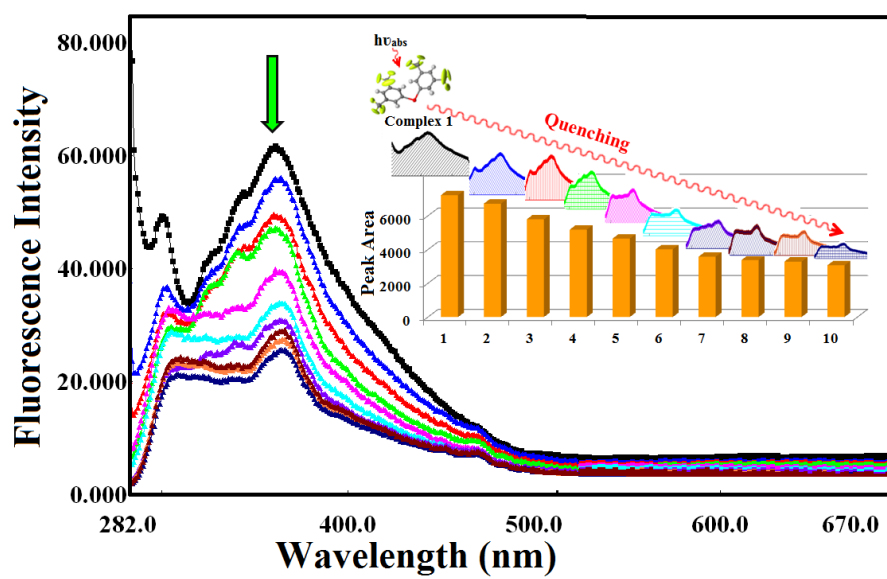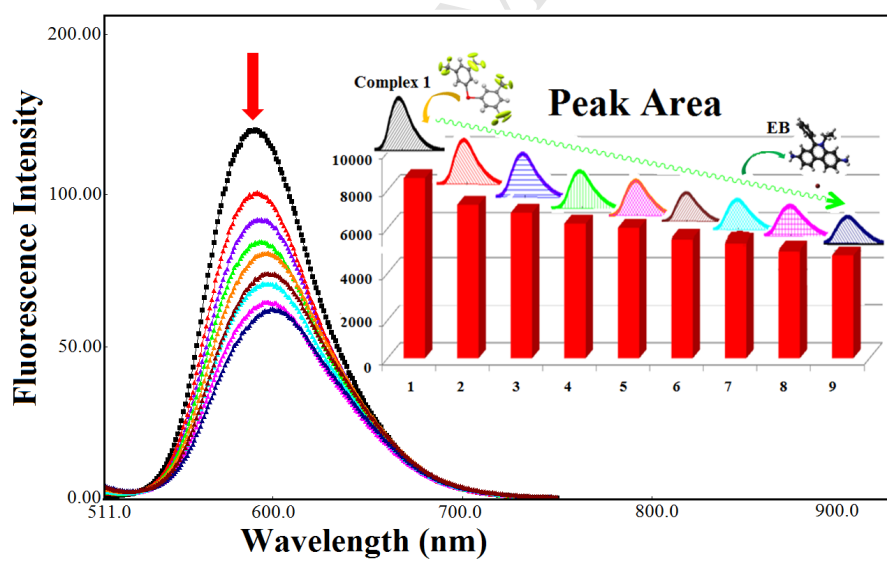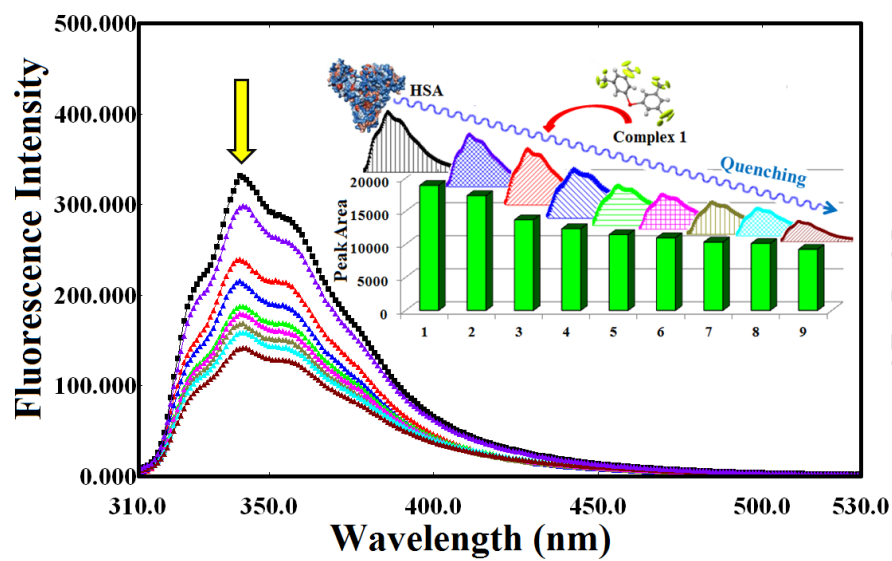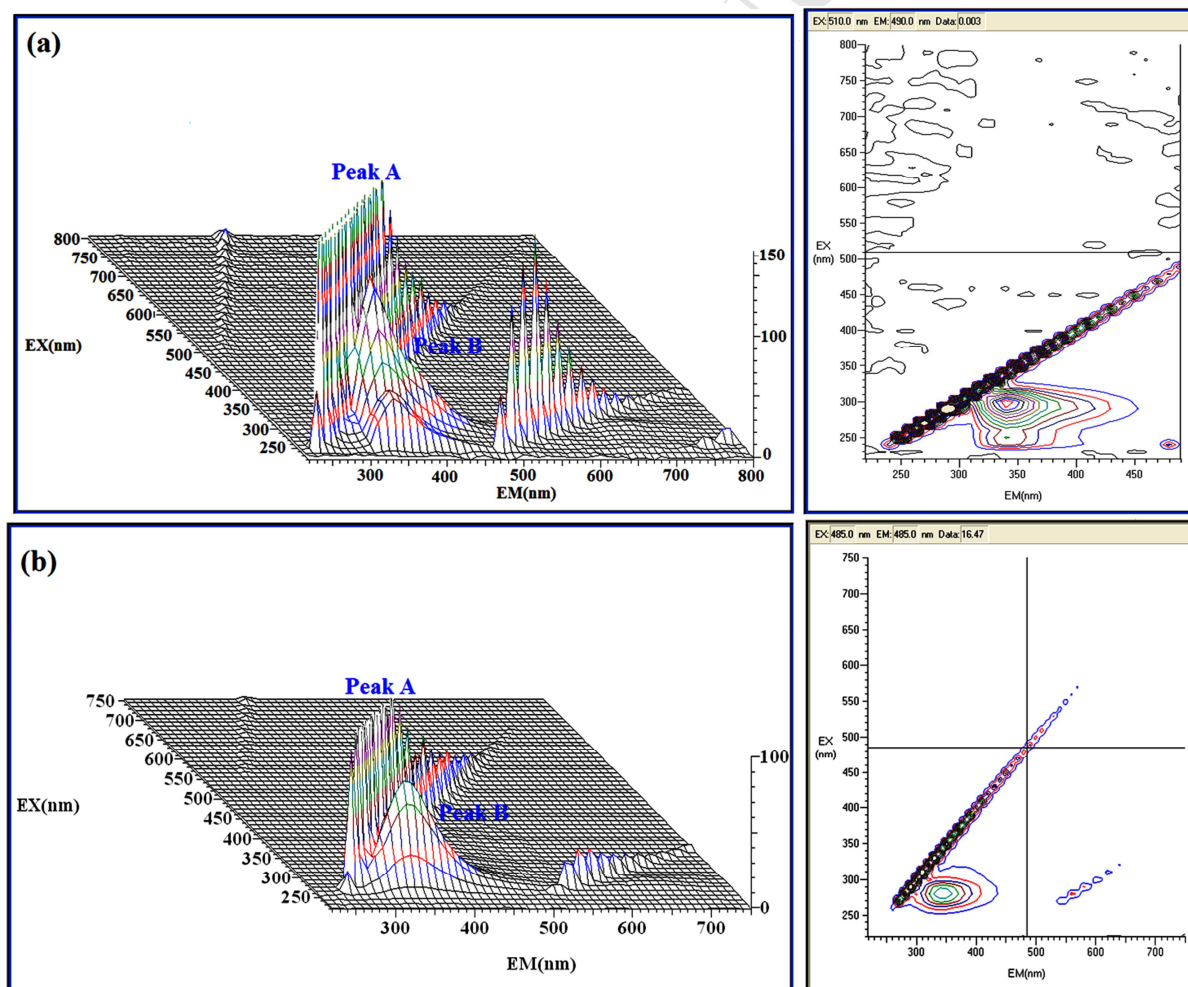
Figure 5

Figure 6

Figure 7

Figure 8

Figure 9

Figure 10

Figure 11

Figure 12

Figure 13

Figure 14

Figure 15

$$\text{Se} + \text{SO}_2\text{Cl}_2 \xrightarrow[0^\circ\text{C}]{\text{THF}} \text{SeCl}_2 + \text{SO}_2 \quad \quad \textbf{(1)}$$

(2)

(3)
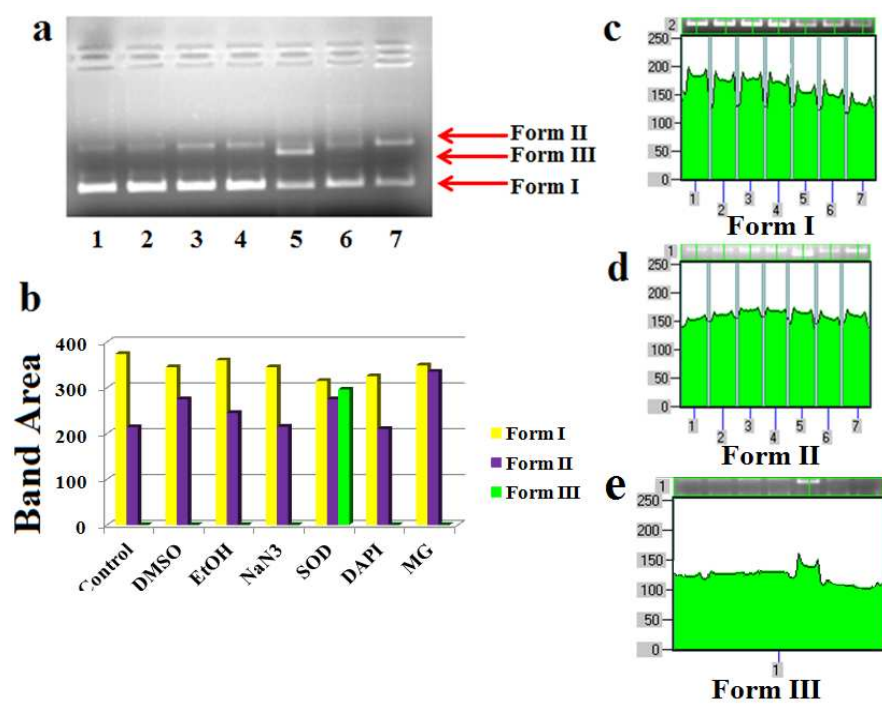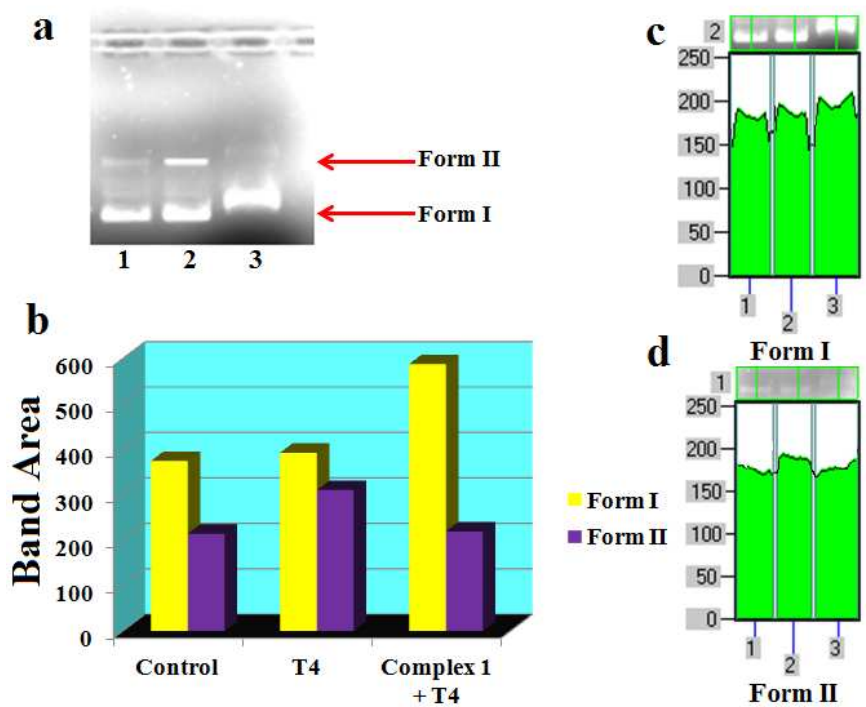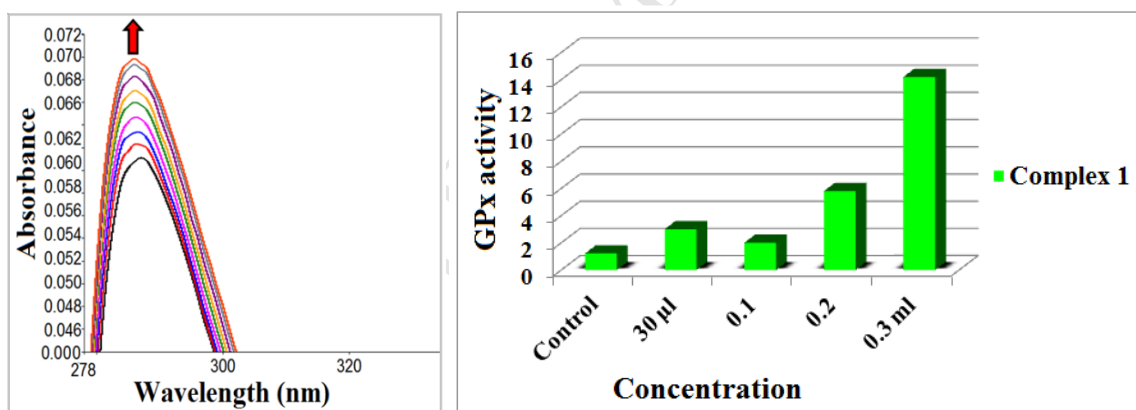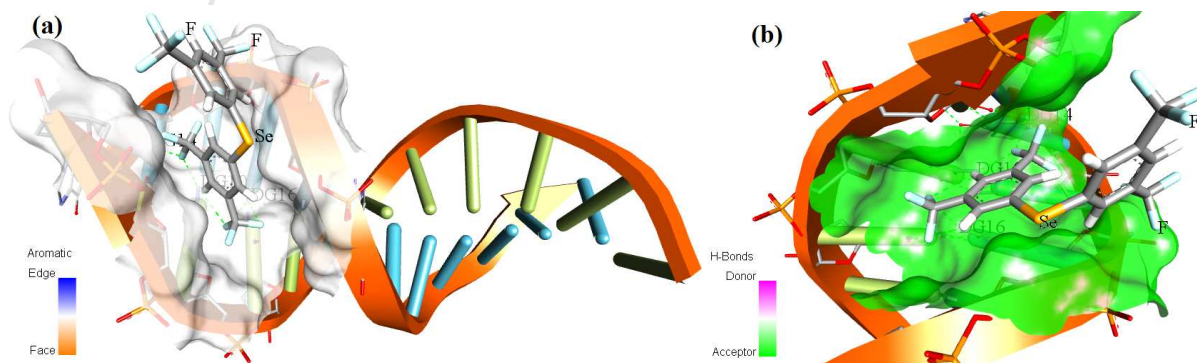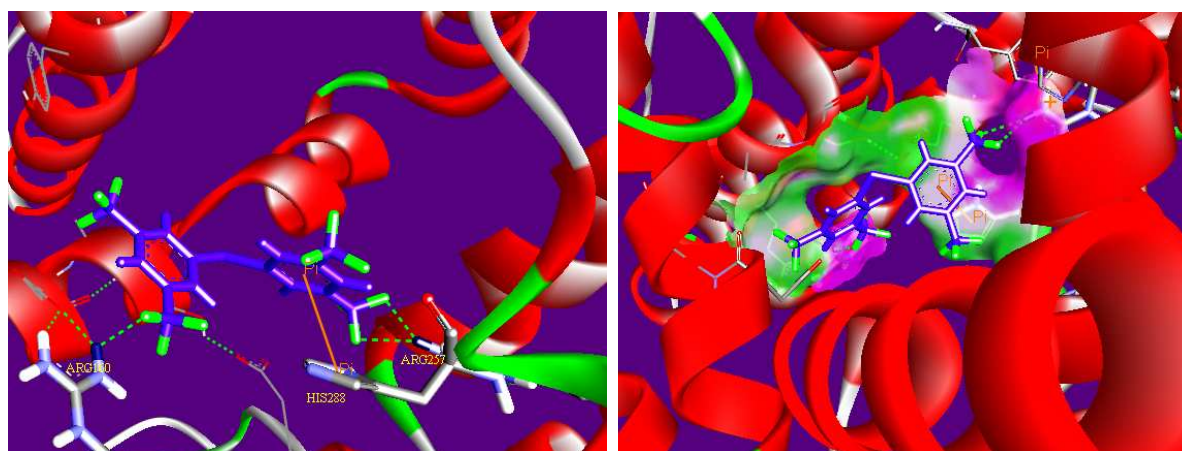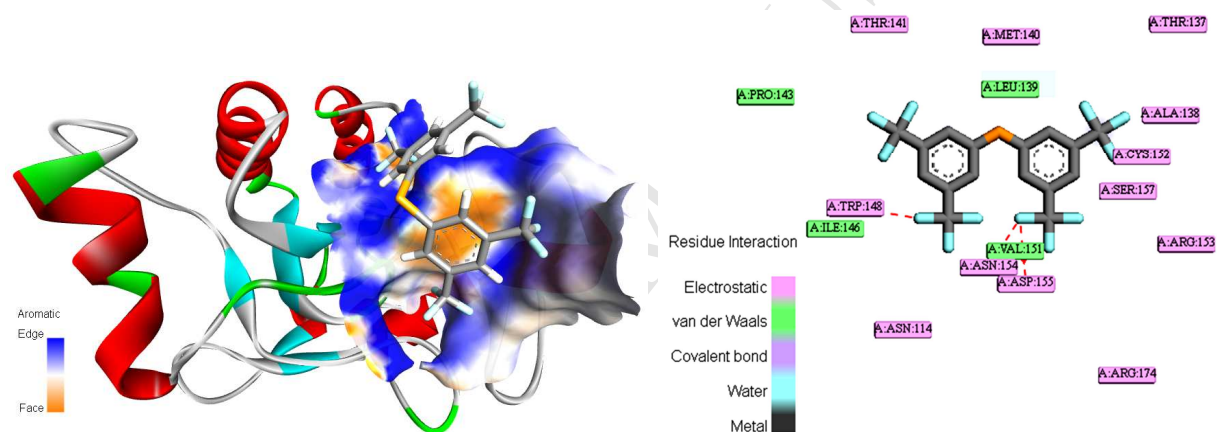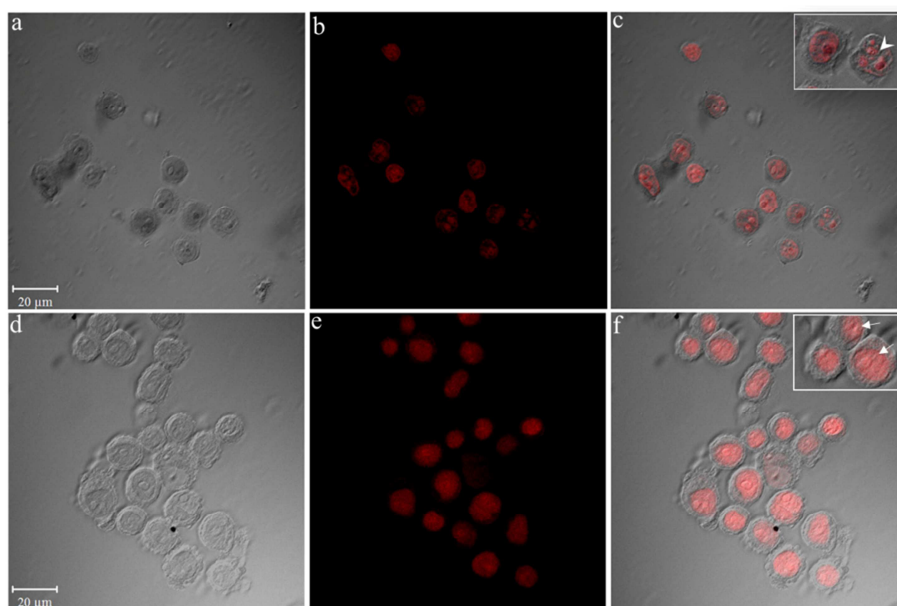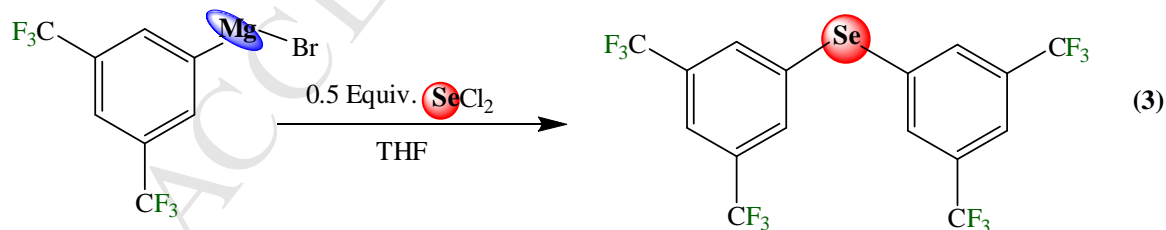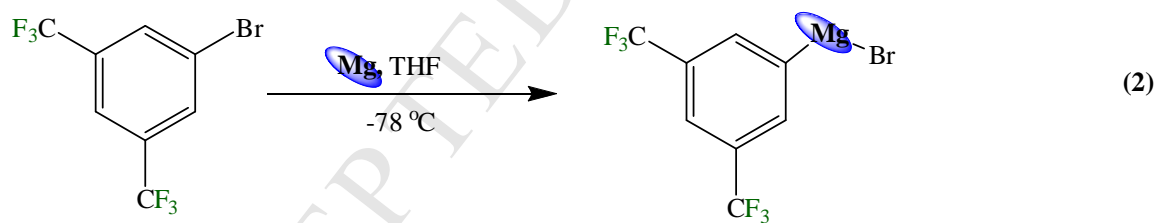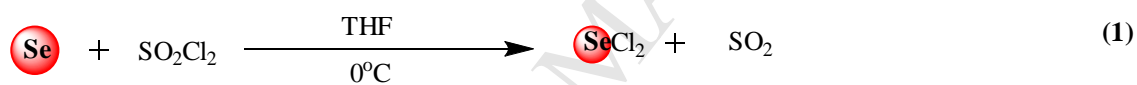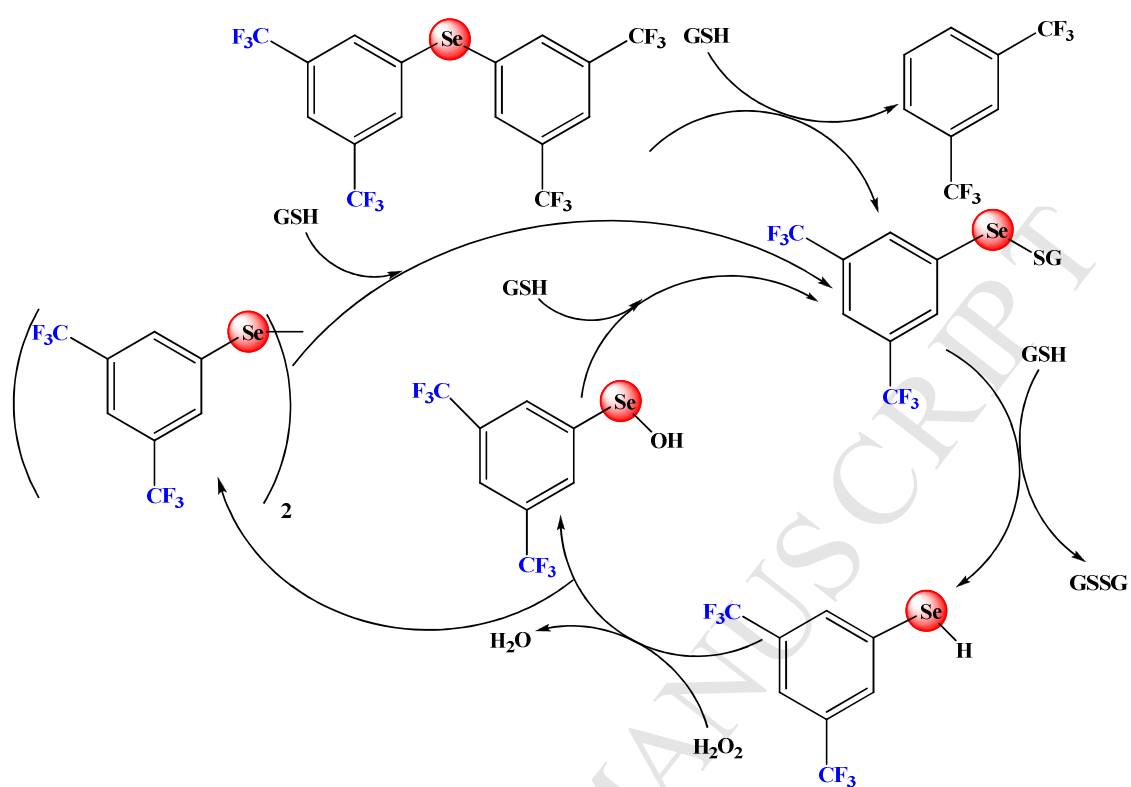
Scheme I

Scheme II

Table 1: Selected Geometrical Parameters (Bond Lengths in Å, Bond Angles in deg) for the Bis(3,5–bis(triflouromethyl)phenyl)selane.

†Geometrical parameter	experimental	Theor. computed using B3LYP functional		
		TZVP	LanL2MB	6–31G
3C—S e	1.917	1.93	1.936	1.942
19 C—Se	1.93	1.93	1.933	1.942
24C—C 29	1.51	1.51	1.50	1.49
25H—F 35	2.445	2.89	2.49	2.48
C3—Se—C19	100.92	100.413	99.531	96.71
C2—C 3—S e	122.41	121.854	120.42	119.45
C29—C 24—C 26	119.61	120.724	120.63	119.60
C20—C 19—Se—C 3[a]	42.26	49.277	47.59	48.34

[a] Dihedral angle. †Atom labeling is based on Fig S1

Table 2: Osiris calculations of compound **1** showing the toxicity risk profile and molecular properties.

Compound	Toxicity risks				Molecular properties				
	MUT	TUM	IRRI	REP	MW	cLogP	S	D–L	D–S
1	🟩	🟩	🟩	🟩	506.0	4.85	–6.66	–27.9	0.17

MUT = Mutagenic, TUM = Tumorigenic, IRRI = Irritant, REP = Reproductive effective

Figure 1
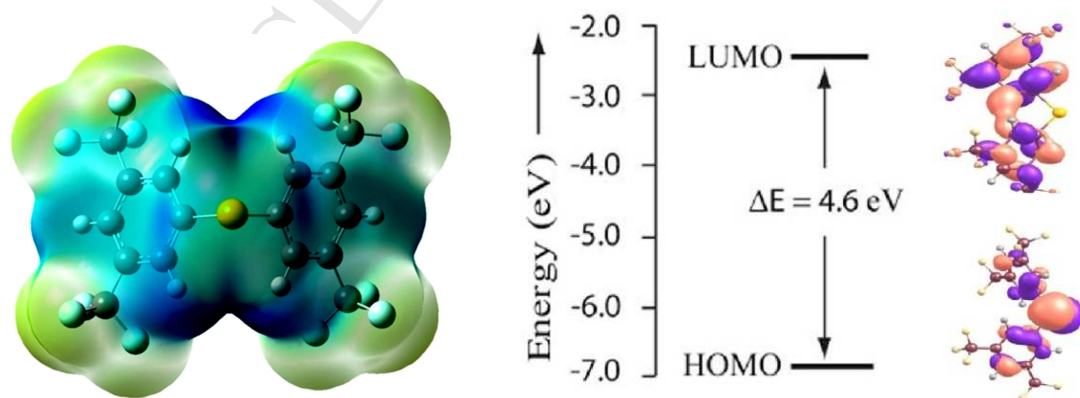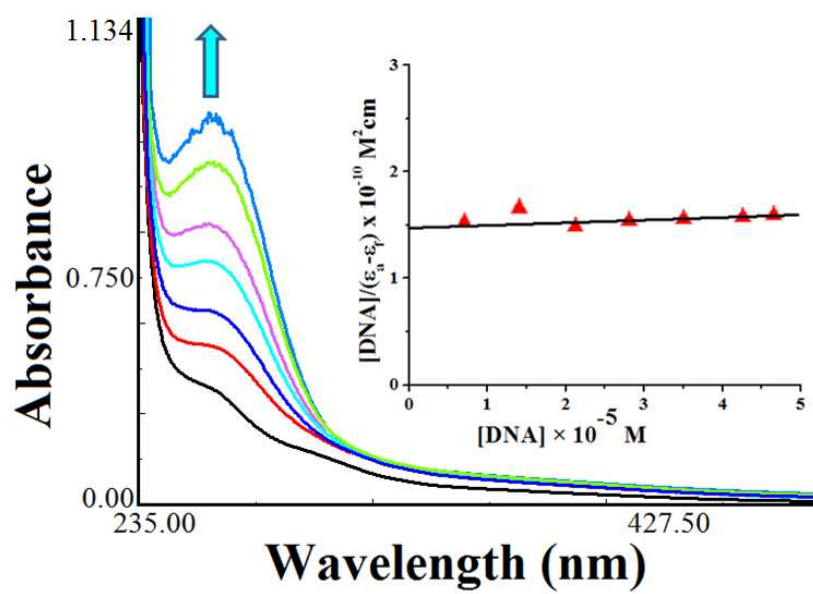

Figure 2

Figure 3

Figure 4
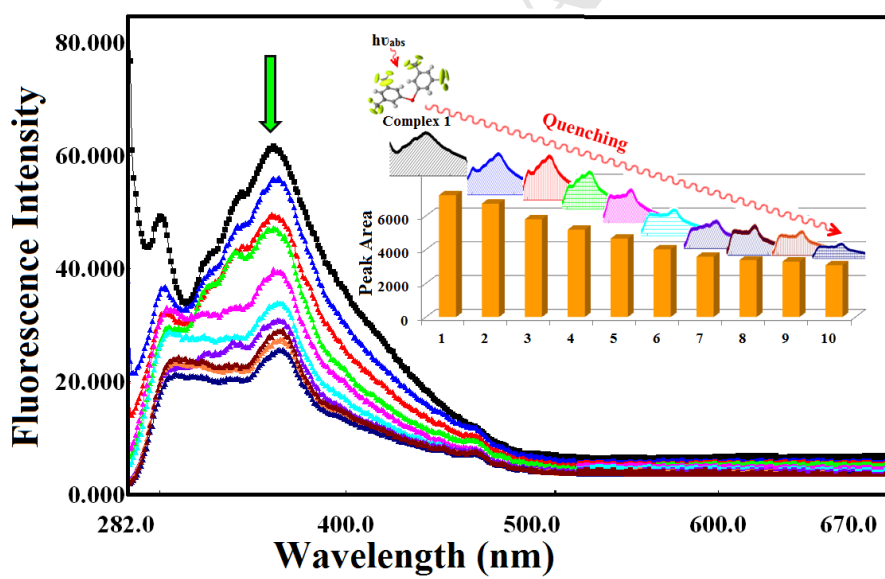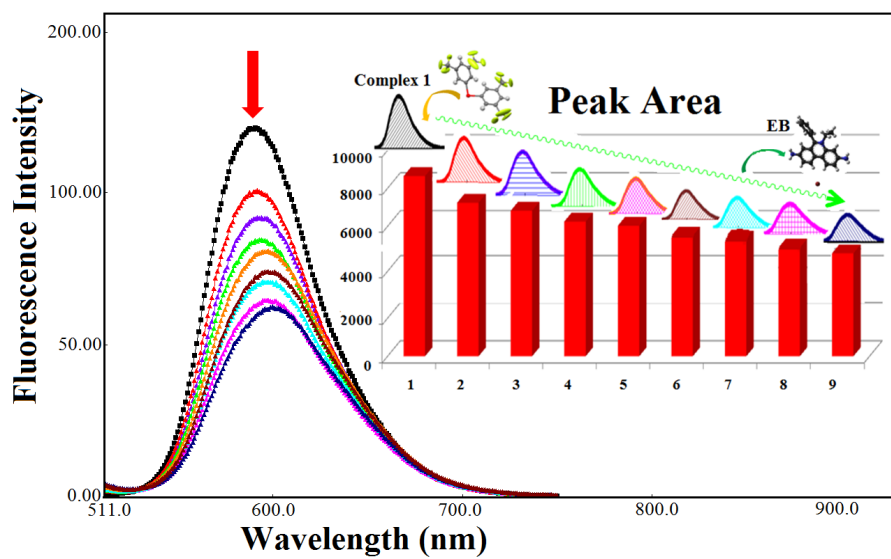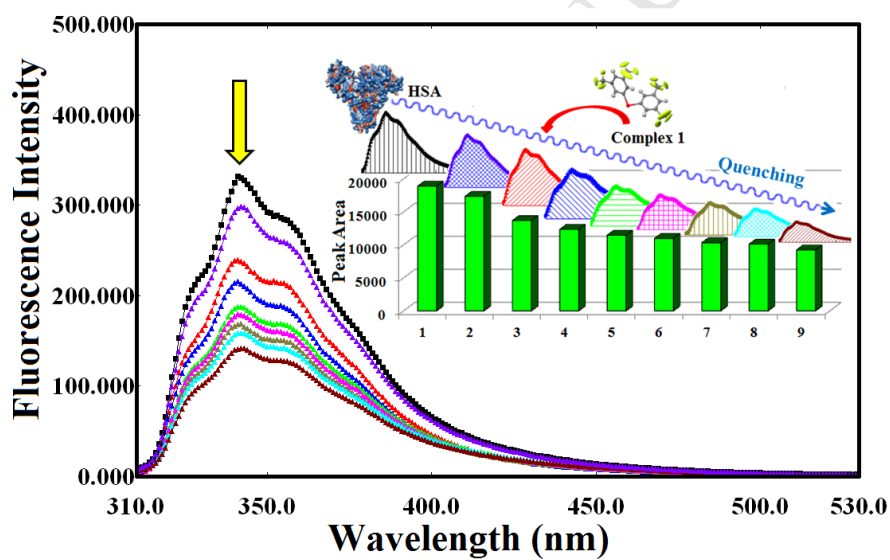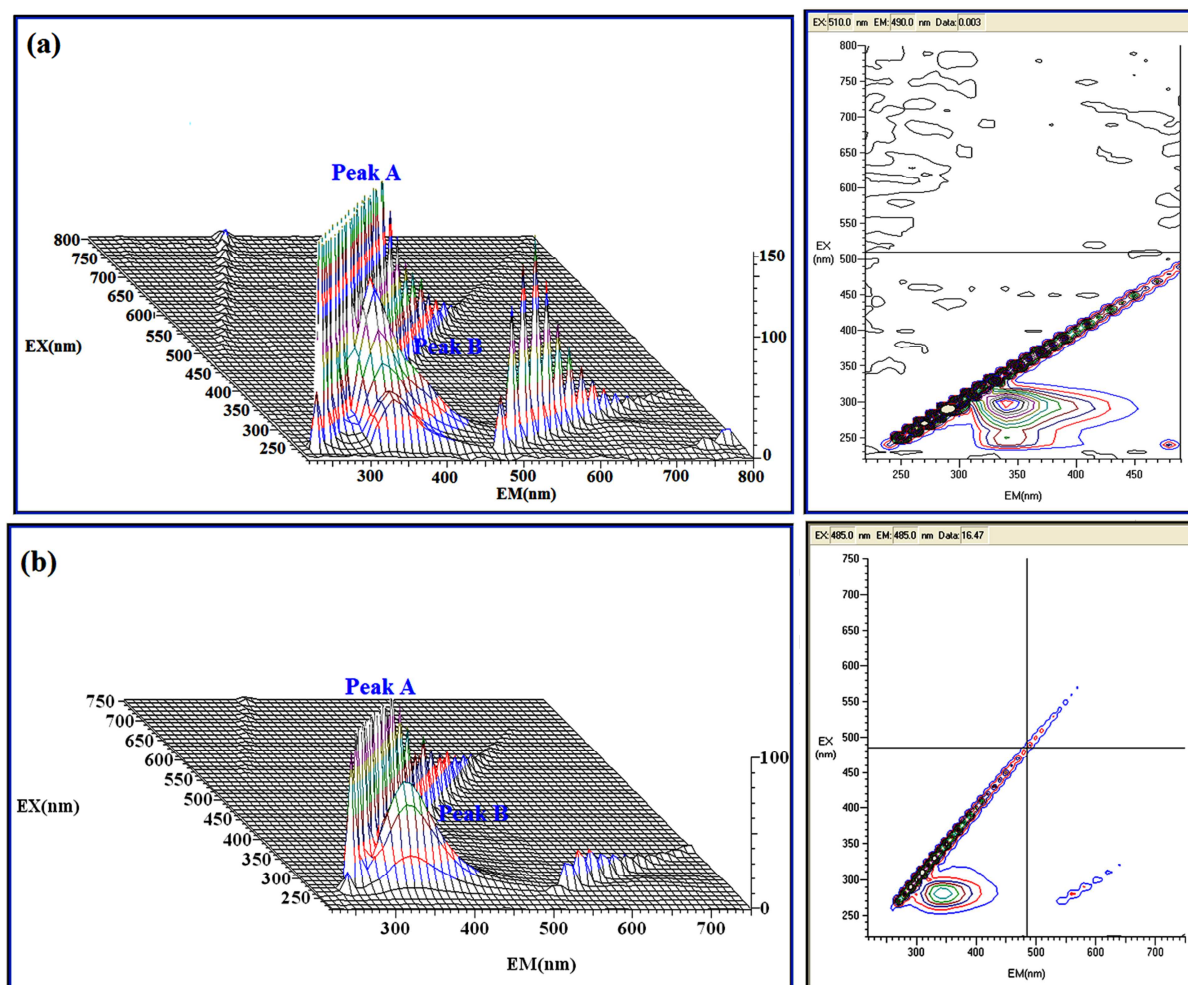
Figure 5

Figure 6

Figure 7

Figure 8

Figure 9

Figure 10

Figure 11

Figure 12

Figure 13

Figure 14

Figure 15

$$Se \quad + \quad SO_2Cl_2 \quad \xrightarrow[0^oC]{THF} \quad SeCl_2 \quad + \quad SO_2 \qquad \textbf{(1)}$$

(2)

(3)
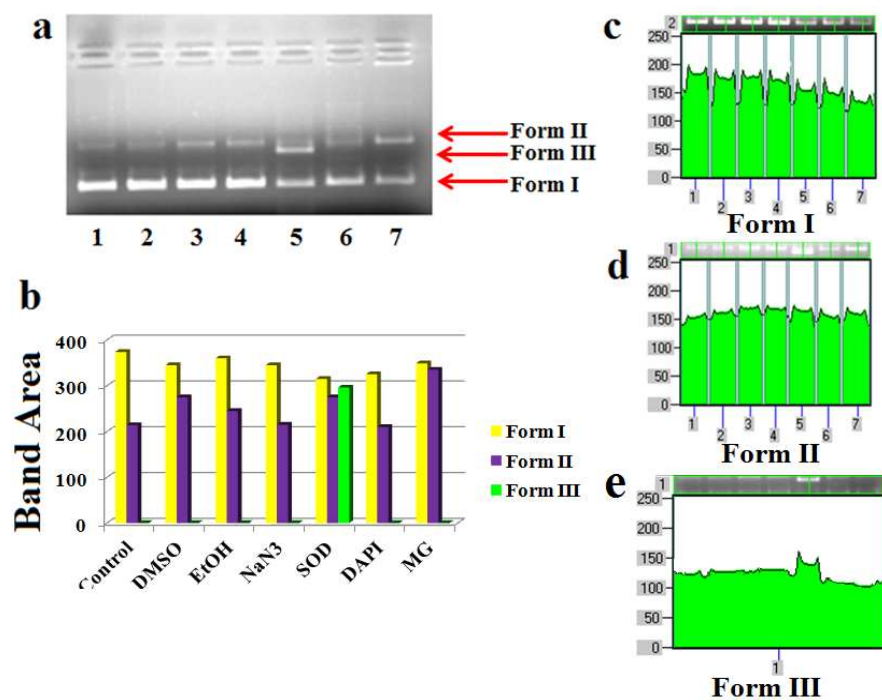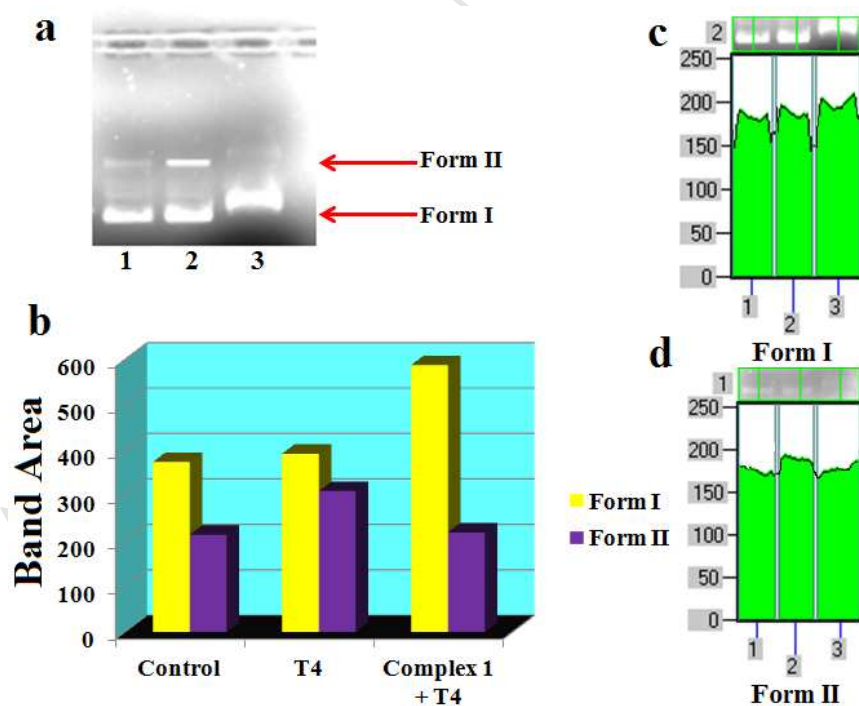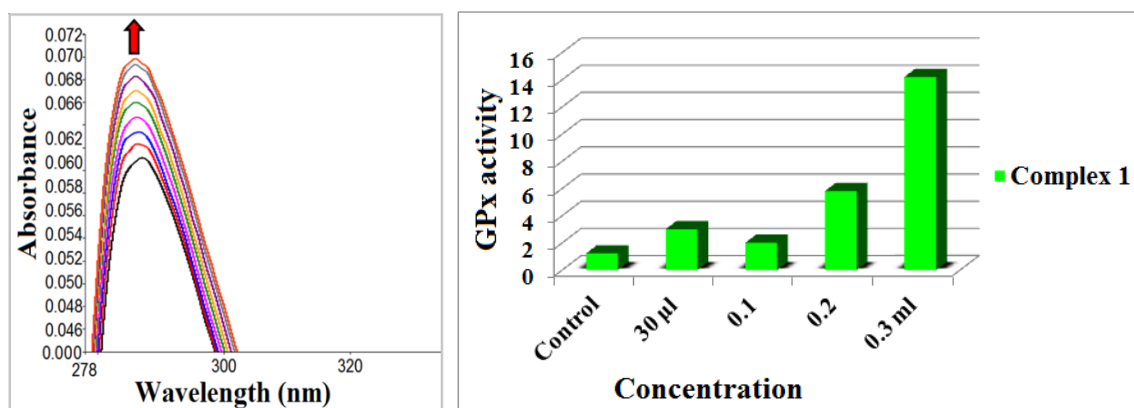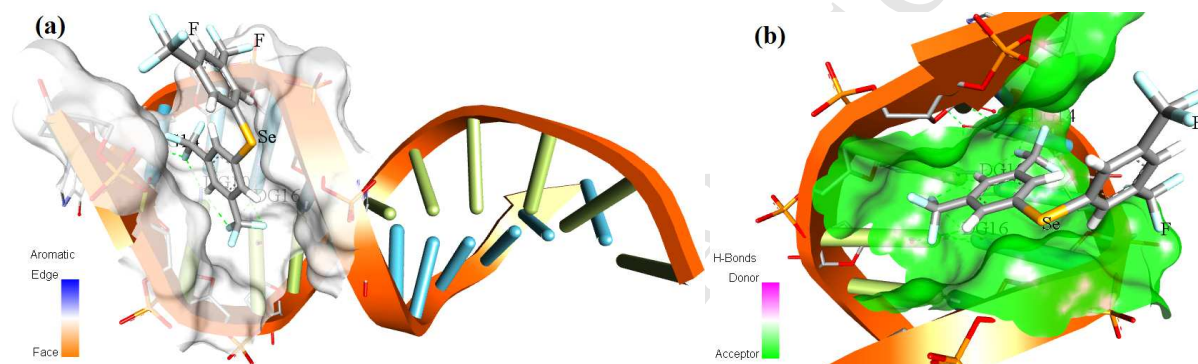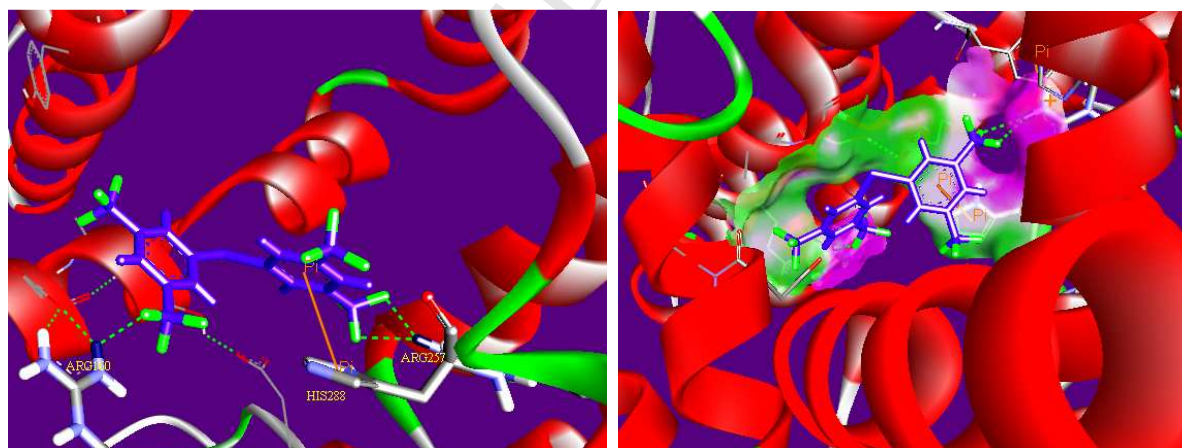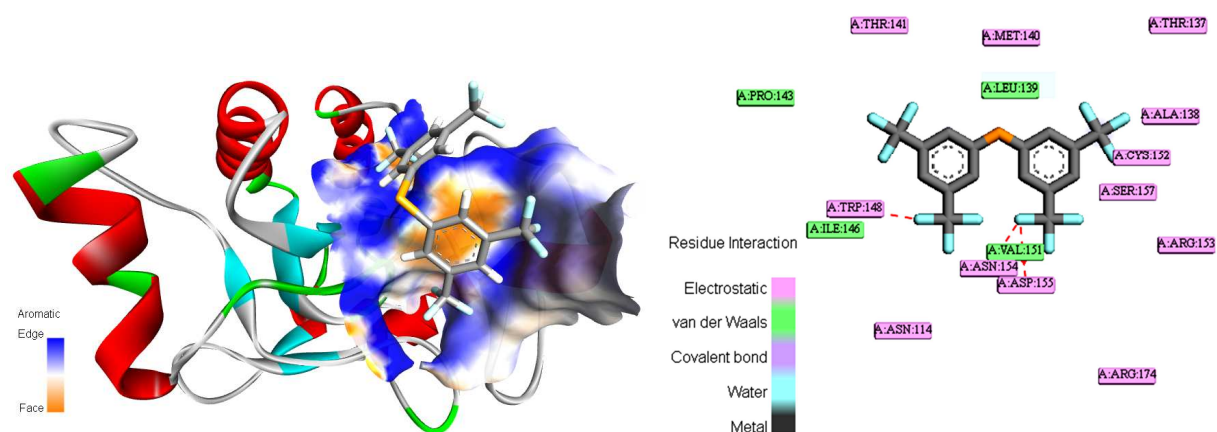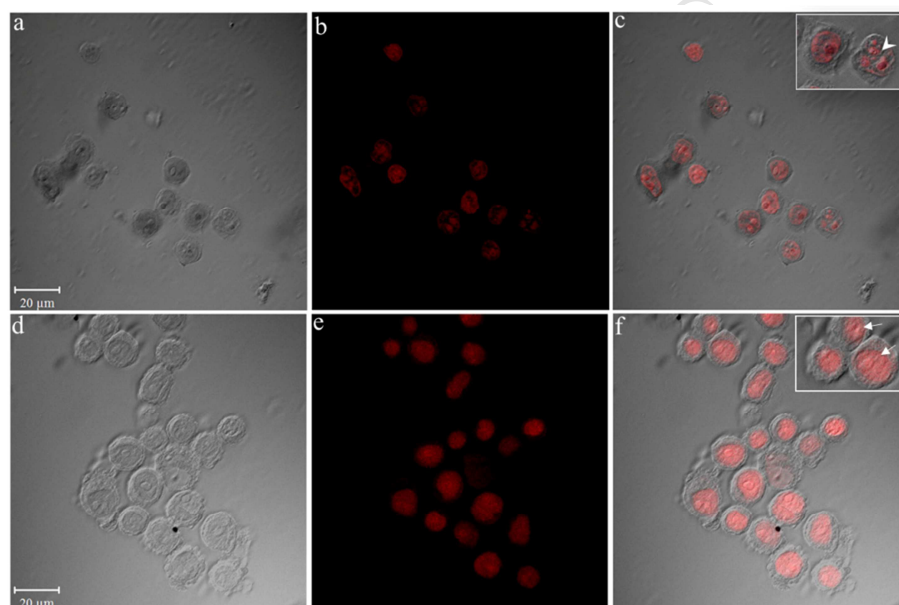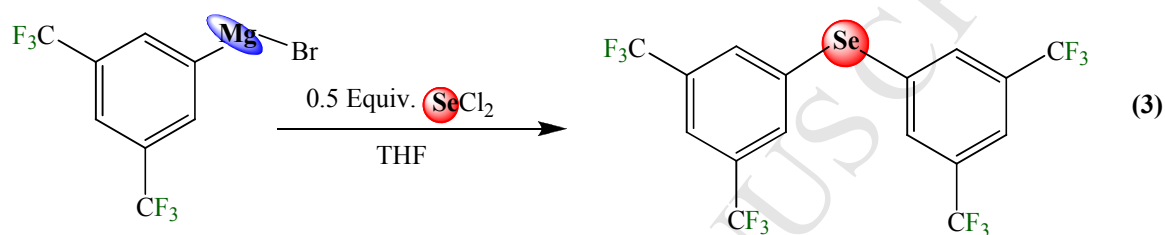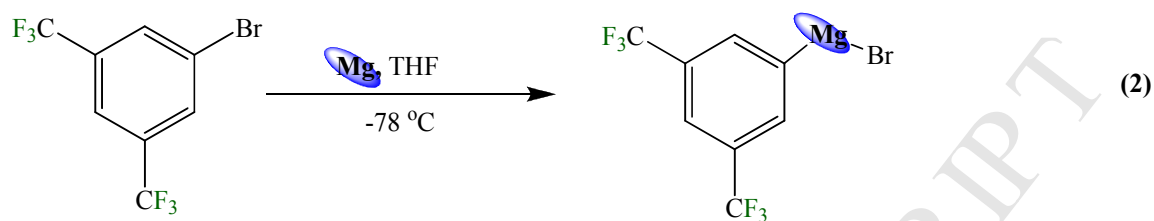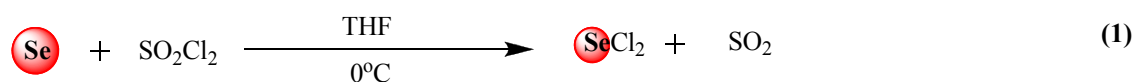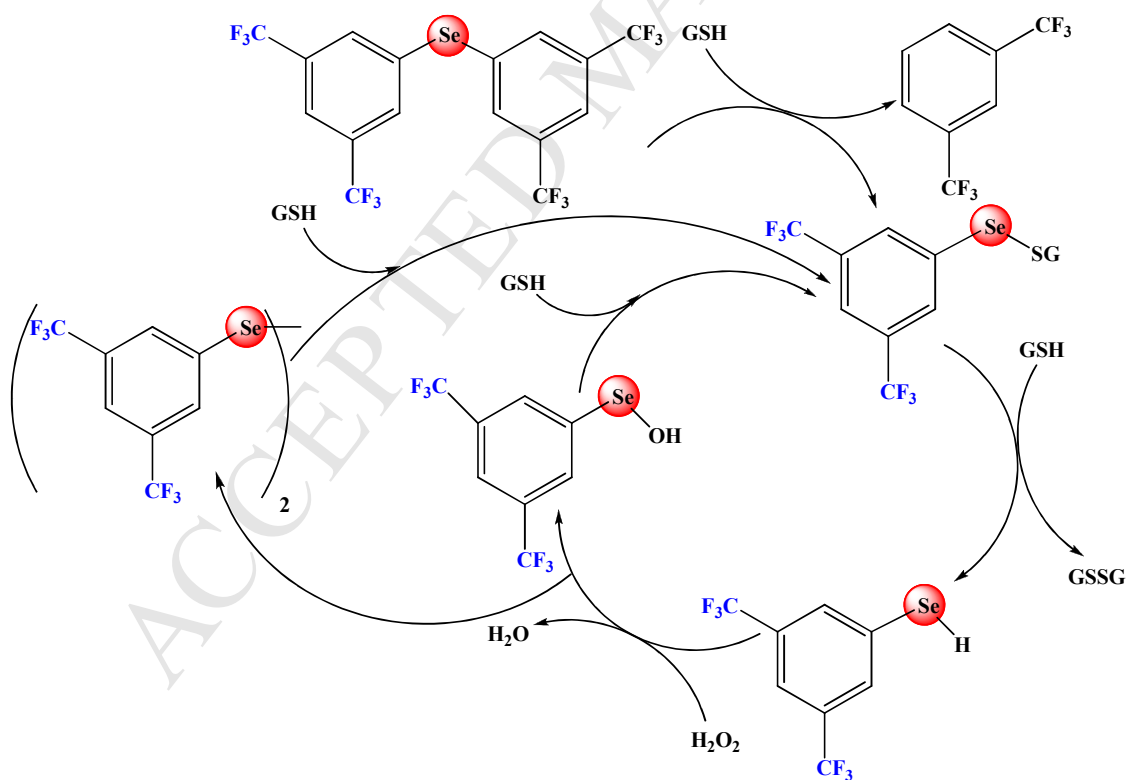
Scheme I

Scheme II

Research Highlights

- New molecular drug candidate was synthesized and characterized.

- DNA/HSA binding studies revealed the electrostatic interaction into the minor groove.

- Compound **1** show single strand cleavage *via* hydrolytic pathway.

- Molecular docking studies revealed minor groove binding in the GC rich sequences.

Supplementary Information

Nuclear blebbing of biologically active organoselenium complex towards human cervical cancer cell (HeLa): *In vitro* DNA/HSA binding, cleavage and cell imaging studies

Masood Ahmad Rizvi,[†] Mehvash Zaki,[‡] Mohd. Afzal,[‡] Manoj Mane,[§] Manjeet Kumar,[‖] Bhahwal Ali Shah,[‖] Saurabh Srivastav,[⊥] Saripella Srikrishna,[⊥] Ghulam Mustafa Peerzada[†] and Sartaj Tabassum[‡]*

[†]*Department of Chemistry, University of Kashmir, Hazratbal, Srinagar–190006, J&K India.*
[‡]Department of Chemistry, Aligarh Muslim University, Aligarh–202002, India
[§]*Centre for Material Characterization, CSIR National Chemical Laboratory (NCL) Pune India.*
[‖]*Natural Product Microbes, CSIR–Indian Institute of Integrative Medicine (IIIM), Jammu Tawi–180001, J&K, India.*
[⊥]*Department of Biochemistry, Faculty of Science, Banaras Hindu University, Varanasi 221005, India*
Corresponding author: Tel.: +91 9358255791
E–mail address: tsartaj62@yahoo.com (S. Tabassum)

Crystallographic Details:

A colorless single crystal (0.552 × 0.332 × 0.241 mm^3) of $C_{16}H_6F_{12}Se$ [bis(3,5-bis(trifluoromethyl)phenyl)selane] was placed in 0.7 mm diameter nylon CryoLoops (Hampton Research) with Paraton-N (Hampton Research). The loop was mounted on a Super Nova Dual source X-ray Diffractometer system (Agilent Technologies) equipped with a CCD area detector and operated at 250 W power (50 kV, 0.8 mA) to generate Mo Kα radiation (λ = 0.71073 Å) and Cu Kα radiation (λ = 1.54178 Å) at 293(2) K. A total of 6955 reflections were collected of which 4721 were unique. The range of θ was from 6.06 to 58.22°. Analysis of the data showed negligible decay during collection. Using Olex2, the structure was solved in P-1 space group, with Z = 2, with the XS structure solution program using Direct Methods and refined with the XL refinement package using Least Squares minimization. All non-hydrogen atoms were refined anisotropically with hydrogen atoms generated as spheres riding the coordinates of their parent atoms. Final full matrix least-squares refinement on F^2 converged to R_1 = 0.0874 [I>2σ (I)] and wR_2 = 0.1801 (all data) with GOF = 1.1.
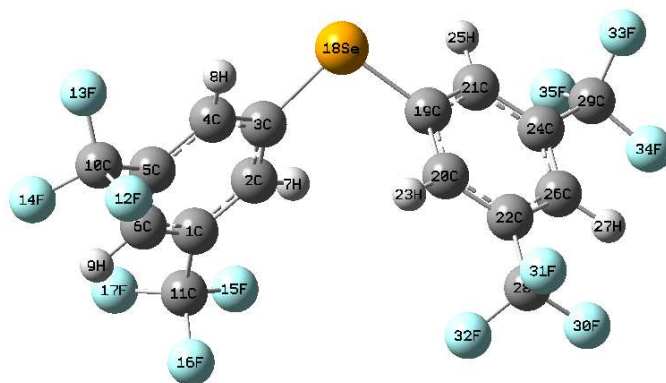
Figure S1. Optimized Structure of Bis(3,5–bis(triflouromethyl)phenyl)selane using B3LYP functional and TZVP basis set.
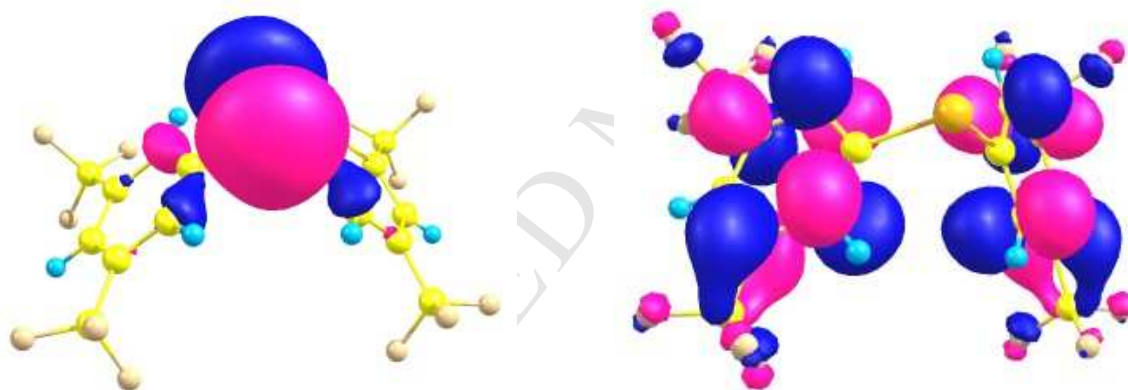
FigureS2. Metal centered HOMO and benzene ring based LUMO molecular orbital's of (3,5–bis(triflouromethyl)phenyl)selane
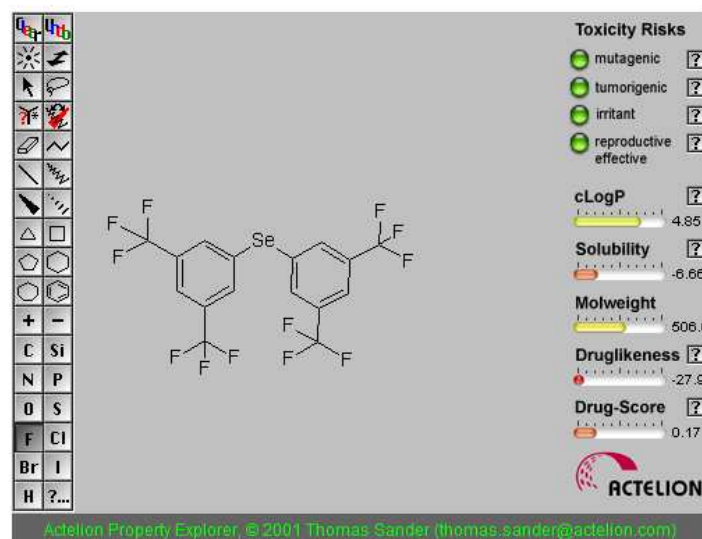
Figure S3. *In vitro* screening of complex **1** by employing the OSIRIS software.
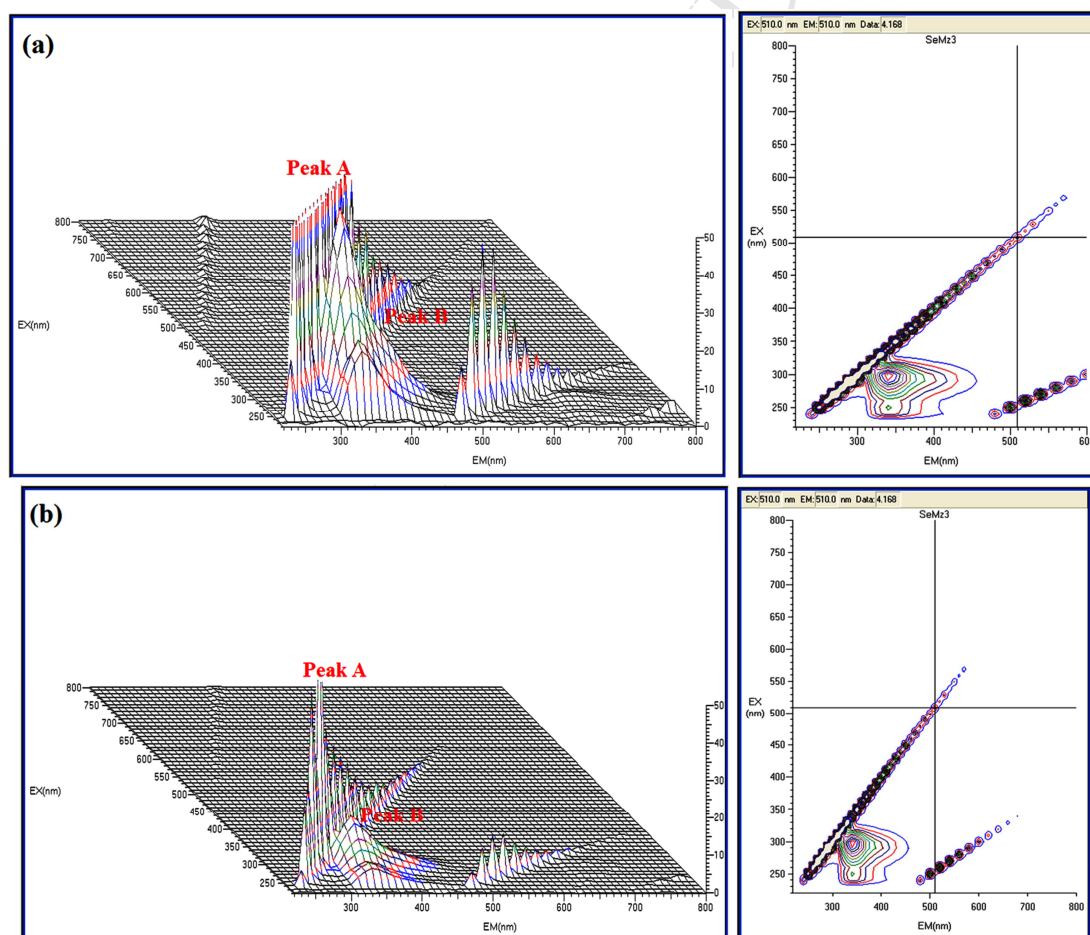
Figure S4. 3D fluorescence spectrum and corresponding contour diagrams of (a) Complex **1** and (b) complex **1**–DNA system. The concentration of complex is fixed at 1.21 mM and that of DNA is fixed at 10.2 mM. pH = 7.3, at room temperature.
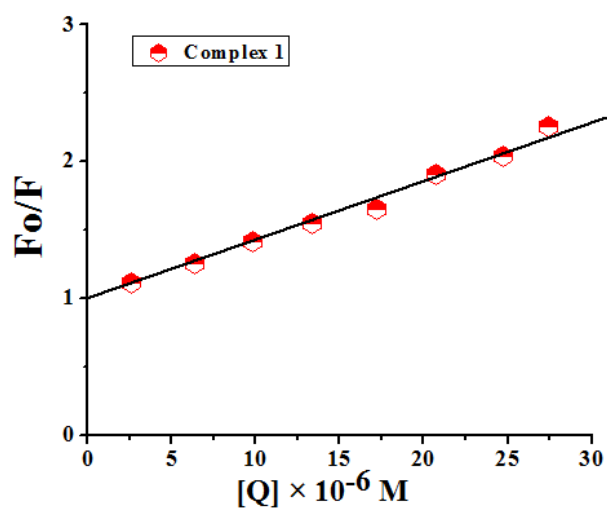
Figure S5. Stern–Volmer plots showing HSA tryptophan quenching caused by complex **1** at room temperature (pH 7.40, λ_{ex} = 295 nm, λ_{em} = 332 nm).
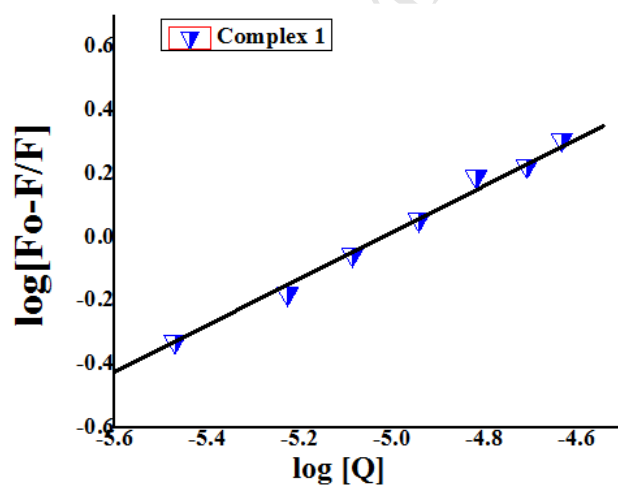
Figure S6. Logarithmic plot of the fluorescence quenching of HSA for the calculation of binding constant (K) and number of binding sites (n) for complex **1** HSA at room temperature.
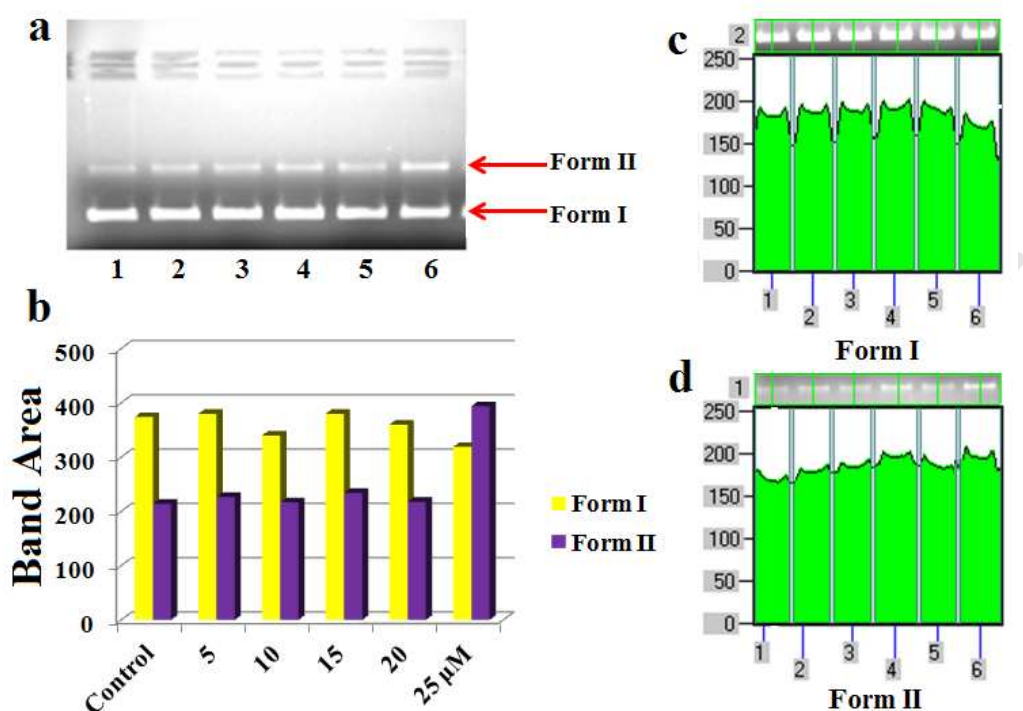
Figure S7. Cleavage of pBR322 plasmid DNA (300ng) by **1** in 50 mM Tris–HCl/NaCl buffer (pH, 7.3) after incubation for 45 min at different concentration (a); Lane 1: DNA control; Lane 2: 5 μM complex **1** + DNA; Lane 3: 10 μM complex **1** + DNA; Lane 4: 15 μM complex **1** + DNA; Lane 5: 20 μM complex **1** + DNA; Lane 6: 25 μM complex **1** + DNA; (b) Quantification of band area in gel electrophoresis originating from Form I and Form II pBR322 plasmid DNA by complex **1** at different concentration. 2D projection of gel images for the cleavage of pBR322 plasmid DNA at different concentration of complex **1**for (c) Form I bands and (d) Form II bands.
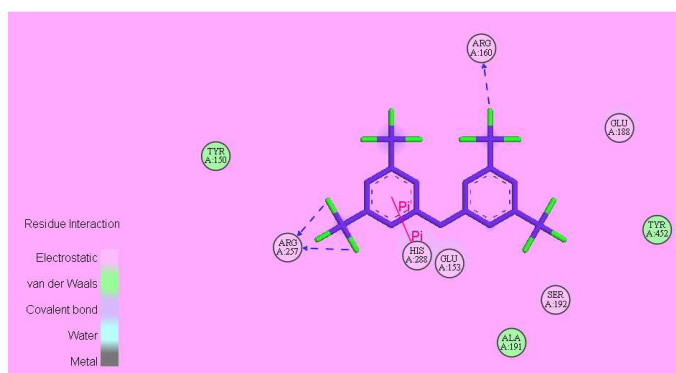
Figure S8. 2D diagram showing electrostatic, van der Waal and π–π interactions of binding site residues with complex **1** in the active site of HSA.
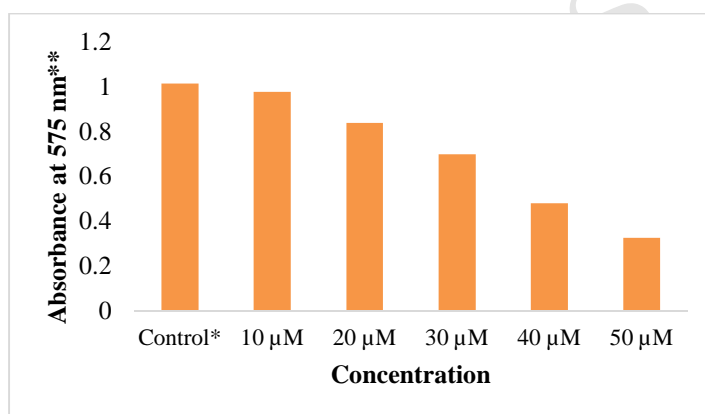
Figure S9. MTT assay of complex **1**. Graph showing effect of complex **1** at different concentration on viability of HeLa cells. More than 50% Cells were viable at ≤30μM, concentration ≥40μM, viability was progressively compromised. *represent control set without complex **1**, ** absorbance corresponds to number of cells.

Analyst
Date

Parshotam
Tuesday, October 08, 2013 1:37 PM
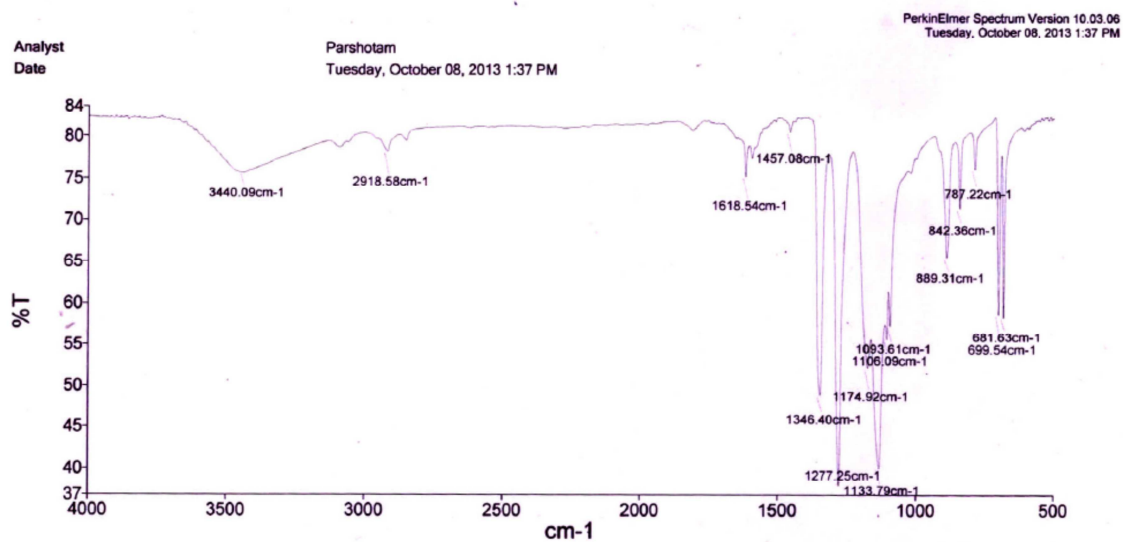
Figure S10. IR Spectra of Bis(3,5–bis(triflouromethyl)phenyl)selane.
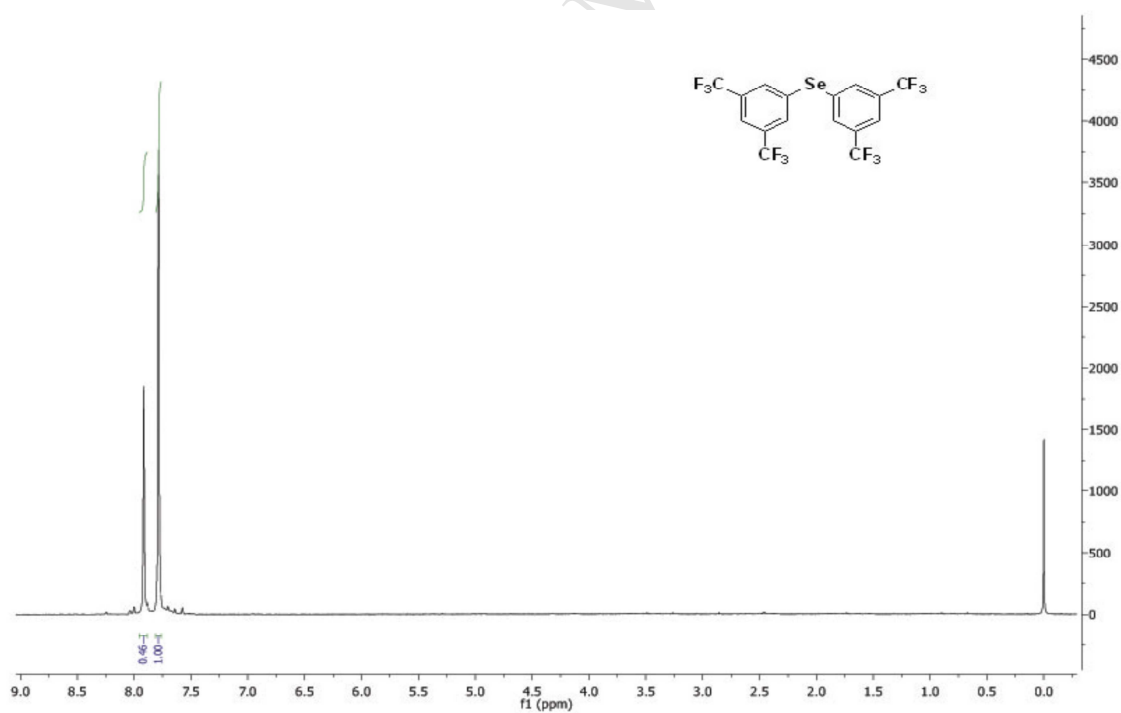
Figure S11. ^{1}H NMR of Bis(3,5–bis(triflouromethyl)phenyl)selane.
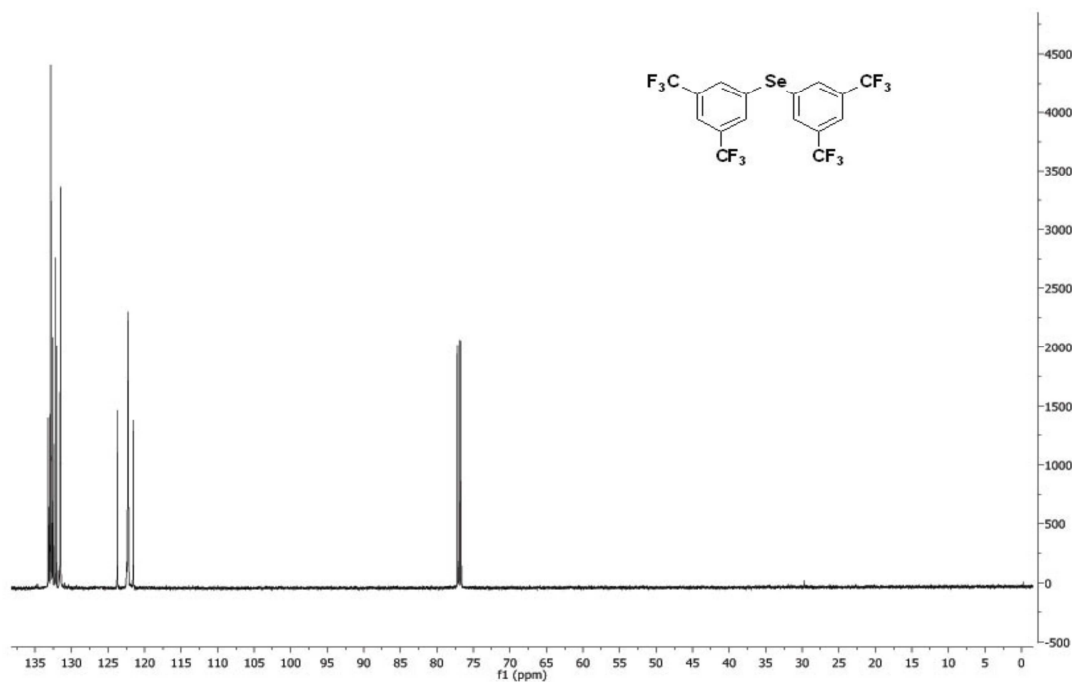
Figure S12. ^{13}C NMR of Bis(3,5–bis(triflouromethyl)phenyl)selane.
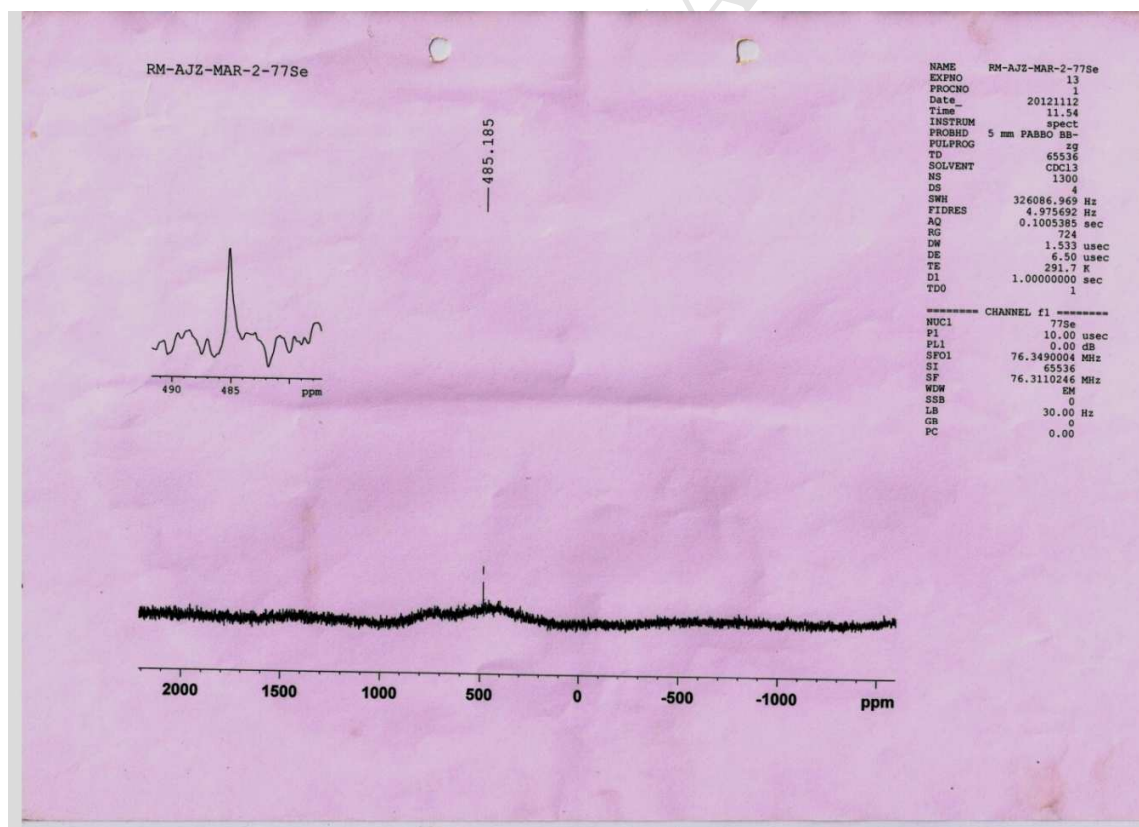
Figure S13. ^{77}Se NMR of Bis(3,5–bis(triflouromethyl)phenyl)selane.
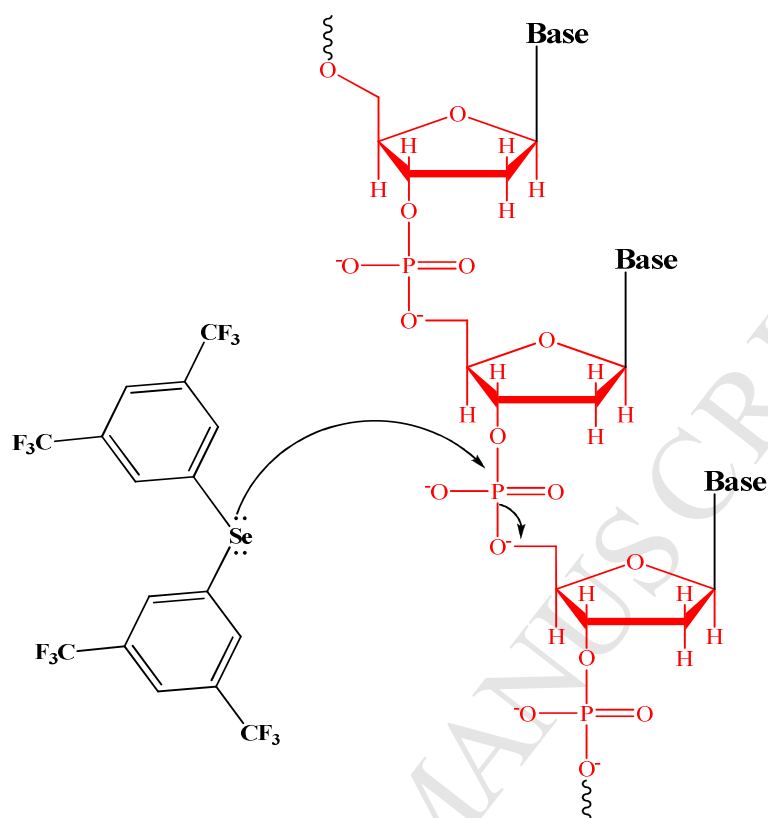
Scheme SI. Proposed intermediate in the hydrolysis of DNA cleavage promoted by complex **1**.

Cartesian coordinates of the Bis (3,5–bis(triflouromethyl)phenyl)selane

C	0.011972	–0.089705	–0.093907
C	–0.039900	–0.001612	1.290704
C	1.147703	0.064157	2.021847
C	2.372683	0.023919	1.364703
C	2.409556	–0.093467	–0.025178
C	1.235075	–0.141145	–0.761303
H	–0.996549	0.009555	1.794481
H	3.296497	0.082358	1.925677
H	1.267609	–0.224802	–1.838872

C	3.746199	–0.097612	–0.728883
C	–1.253692	–0.139122	–0.916207
F	4.241073	1.155191	–0.858046
F	4.667333	–0.812182	–0.047979
F	3.662576	–0.620262	–1.967515
F	–2.361556	–0.158297	–0.150800
F	–1.349332	0.932041	–1.735643
F	–1.288187	–1.236480	–1.704019
Se	1.155354	0.097690	3.960830
C	–0.200841	1.444365	4.293612
C	–0.188218	2.678463	3.646265
C	–1.162260	1.181670	5.266053
C	–1.150599	3.632685	3.962630
H	0.563109	2.897638	2.898838
C	–2.103497	2.156144	5.591548
H	–1.187757	0.218735	5.760427
C	–2.107868	3.383556	4.941732
H	–2.847426	4.131431	5.187039
C	–1.116469	4.960779	3.242536
C	–3.125171	1.842997	6.659729
F	–2.172449	5.735342	3.552986
F	–0.000761	5.661583	3.548099
F	–1.116545	4.795363	1.900967
F	–2.539408	1.662075	7.864966
F	–4.035962	2.823554	6.801161
F	–3.798290	0.704366	6.379477

Table S1. Crystal data and structure refinement of Bis(3,5–bis(triflouromethyl)phenyl)selane.

Empirical formula	$C_{16}H_6F_{12}Se$
Formula weight	505.17
Temperature	293(2)
Wavelength	0.71073 Å (Mo)
Crystal system	triclinic
Space group	P–1
Unit cell dimensions	$a = 8.7402(5)$ Å, $\alpha = 107.674(4)°$
	$b = 8.9544(5)$ Å , $\beta = 102.497(4)°$
	$c = 12.4403(6)$ Å, $\gamma = 99.079(5)°$
Volume	879.16(9)
Z	2
Density (calculated)	1.908
Absorption coefficient	2.256
F (000)	488.0
Crystal size	$0.552 \times 0.332 \times 0.241$ mm^3
Theta range for data collection	6.06 to 58.22°
Index ranges	$-10 \le h \le 11, -12 \le k \le 10, -14 \le l \le 17$
Reflections collected	6955
Independent reflections	4721[R(int) = 0.0216]
Completeness to theta = 58.22°	97%
Absorption correction	Semi–empirical from equivalents
Refinement method	Full–matrix least–squares on F2
Data / restraints / parameters	4721/0/262
Goodness–of–fit on F2	3.263
Final R indices [I>2σ(I)]	$R_1 = 0.0874$, $wR_2 = 0.1801$
R indices (all data)	$R_1 = 0.1007$, $wR_2 = 0.1824$
Largest diff. peak and hole	1.52 and -1.09 eÅ^{-3}

Table S2 Fractional Atomic Coordinates ($\times 10^4$) and Equivalent Isotropic Displacement Parameters ($\text{Å}^2 \times 10^3$) for Bis(3,5–bis(triflouromethyl)phenyl)selane. U_{eq} is defined as 1/3 of the trace of the orthogonalised U_{IJ} tensor.

Atom	x	y	z	U(eq)
Se1	4353.5(9)	3152.2(8)	2179.6(5)	50.6(3)
F1	1341(7)	-3847(10)	-1399(6)	217(5)
F5	8072(10)	-1538(13)	1159(8)	223(6)
F14	10601(5)	7518(5)	6251(4)	77.1(13)
F26	7698(7)	-1498(8)	2668(5)	132(2)
F28	8637(6)	8589(5)	6373(6)	124(2)
F29	6685(8)	-3485(7)	1313(9)	214(5)
F41	6870(8)	1021(6)	5813(5)	120(2)
F44	8033(10)	2975(8)	7227(5)	197(4)
F45	5598(10)	2412(11)	6658(8)	196(5)
F52	251(8)	-2131(9)	-986(8)	195(4)
F53	9404(8)	7987(7)	4818(5)	151(3)
F58	408(12)	-3529(16)	-95(8)	297(8)
C3	4285(7)	894(7)	1588(4)	36.1(14)
C4	5845(7)	3797(7)	3705(5)	35.5(14)
C6	5639(7)	297(7)	1816(4)	36.2(14)
C9	8023(7)	5845(7)	5205(5)	37.3(14)
C11	5819(7)	2900(7)	4428(5)	36.1(14)
C13	6959(7)	5262(7)	4089(5)	36.1(14)
C15	8012(7)	4940(7)	5925(5)	37.2(14)
C17	5518(8)	-1356(7)	1292(5)	36.5(14)
C22	6922(7)	3473(7)	5536(5)	34.3(14)
C23	4085(7)	-2368(7)	538(5)	35.7(14)
C25	2839(8)	-135(8)	841(5)	42.5(16)
C27	2756(8)	-1753(8)	310(5)	40.5(15)
C37	9171(9)	7487(9)	5653(7)	58(2)
C7	6884(11)	2499(9)	6317(6)	58(2)
C2	7012(11)	-1946(10)	1572(7)	63(2)
C1	1218(10)	-2807(10)	-517(7)	67(2)

Table S3 Anisotropic Displacement Parameters ($\text{Å}^2 \times 10^3$) for compound 1. The Anisotropic displacement factor exponent takes the form: $-2\pi^2[h^2a^{*2}U_{11}+...+2hka \times b \times U_{12}]$

Atom	U_{11}	U_{22}	U_{33}	U_{23}	U_{13}	U_{12}
Se1	63.6(5)	40.4(4)	34.2(4)	2.7(3)	-5.8(3)	22.8(3)
F1	71(4)	213(8)	172(6)	-152(6)	-46(4)	38(5)
F5	183(7)	442(15)	320(10)	332(11)	209(8)	257(9)
F14	48(3)	51(3)	97(3)	8(2)	-11(2)	-3(2)
F26	124(5)	166(6)	94(4)	38(4)	-21(3)	84(5)
F28	81(4)	32(3)	228(7)	-2(3)	57(4)	7(3)
F29	109(5)	51(4)	365(11)	-4(5)	-78(6)	43(4)
F41	214(7)	66(4)	107(4)	58(3)	42(4)	52(4)
F44	228(8)	163(6)	116(5)	116(5)	-107(5)	-108(6)
F45	229(9)	313(11)	278(10)	268(9)	210(8)	187(8)
F52	102(5)	108(6)	235(8)	-30(5)	-102(5)	18(4)
F53	159(6)	118(5)	125(5)	87(4)	-43(4)	-81(4)
F58	197(9)	396(16)	150(7)	134(9)	-81(6)	-232(11)
C3	43(4)	39(4)	23(3)	10(3)	6(3)	7(3)
C4	37(4)	37(4)	29(3)	4(3)	7(2)	18(3)
C6	46(4)	35(4)	22(3)	8(2)	3(3)	7(3)
C9	27(3)	37(4)	45(4)	9(3)	8(3)	11(3)
C11	33(4)	29(3)	39(3)	5(3)	8(3)	5(3)
C13	43(4)	39(4)	29(3)	15(3)	8(3)	12(3)
C15	46(4)	38(4)	25(3)	9(3)	3(3)	15(3)
C17	54(4)	37(4)	24(3)	16(3)	12(3)	13(3)
C22	41(4)	34(3)	30(3)	9(3)	13(3)	14(3)
C23	50(4)	31(3)	28(3)	13(3)	15(3)	4(3)
C25	50(4)	46(4)	30(3)	13(3)	10(3)	11(3)
C27	47(4)	41(4)	28(3)	11(3)	10(3)	0(3)
C37	51(5)	40(4)	72(5)	19(4)	3(4)	3(4)
C7	93(6)	45(5)	42(4)	21(3)	23(4)	14(4)
C2	97(7)	56(5)	47(4)	17(4)	20(4)	47(5)
C1	58(6)	62(6)	62(5)	21(4)	-1(4)	-12(4)

Table S4 Bond Lengths for Bis(3,5–bis(triflouromethyl)phenyl)selane.

Atom	Atom	Length/Å	Atom	Atom	Length/Å
Se1	C3	1.916(6)	C3	C25	1.384(8)
Se1	C4	1.913(5)	C4	C11	1.378(8)
F1	C1	1.243(9)	C4	C13	1.383(8)
F5	C2	1.212(9)	C6	C17	1.401(8)
F14	C37	1.300(8)	C9	C13	1.383(7)
F26	C2	1.271(8)	C9	C15	1.379(8)
F28	C37	1.336(8)	C9	C37	1.508(9)
F29	C2	1.285(9)	C11	C22	1.389(7)
F41	C7	1.278(8)	C15	C22	1.374(8)
F44	C7	1.246(8)	C17	C23	1.373(8)
F45	C7	1.284(9)	C17	C2	1.496(9)
F52	C1	1.258(10)	C22	C7	1.493(8)
F53	C37	1.291(8)	C23	C27	1.374(8)
F58	C1	1.191(10)	C25	C27	1.380(8)
C3	C6	1.383(8)	C27	C1	1.473(9)

Table S5 Bond Angles for Bis(3,5–bis(triflouromethyl)phenyl)selane.

Atom	Atom	Atom	Angle/°	Atom	Atom	Atom	Angle/°
C4	Se1	C3	100.9(2)	F14	C37	F28	106.0(6)
C6	C3	Se1	122.4(4)	F14	C37	C9	113.0(6)
C6	C3	C25	120.0(6)	F28	C37	C9	111.2(6)
C25	C3	Se1	117.4(5)	F53	C37	F14	105.2(7)
C11	C4	Se1	123.2(5)	F53	C37	F28	108.1(7)
C11	C4	C13	119.8(5)	F53	C37	C9	112.8(6)
C13	C4	Se1	117.0(4)	F41	C7	F45	103.4(8)
C3	C6	C17	119.2(6)	F41	C7	C22	113.4(6)
C13	C9	C37	120.4(6)	F44	C7	F41	104.6(8)
C15	C9	C13	120.0(6)	F44	C7	F45	106.0(8)
C15	C9	C37	119.6(6)	F44	C7	C22	115.7(7)
C4	C11	C22	119.6(6)	F45	C7	C22	112.6(7)
C4	C13	C9	120.3(5)	F5	C2	F26	104.5(9)
C22	C15	C9	119.7(5)	F5	C2	F29	109.9(8)
C6	C17	C2	117.2(6)	F5	C2	C17	115.9(6)

C23	C17	C6	120.5(6)	
C23	C17	C2	122.2(6)	
C11	C22	C7	119.3(6)	
C15	C22	C11	120.7(5)	
C15	C22	C7	120.0(5)	
C17	C23	C27	119.6(6)	
C27	C25	C3	119.9(6)	
C23	C27	C25	120.8(6)	
C23	C27	C1	120.5(6)	
C25	C27	C1	118.7(6)	

F26	C2	F29	99.9(7)
F26	C2	C17	113.5(6)
F29	C2	C17	111.7(7)
F1	C1	F52	101.0(8)
F1	C1	C27	115.3(8)
F52	C1	C27	116.7(7)
F58	C1	F1	105.3(10)
F58	C1	F52	102.4(10)
F58	C1	C27	114.3(8)

Table S6 Torsion Angles for Bis(3,5–bis(triflouromethyl)phenyl)selane.

A	B	C	D	Angle/°
Se1	C3	C6	C17	-176.0(4)
Se1	C3	C25	C27	174.6(4)
Se1	C4	C11	C22	-178.5(4)
Se1	C4	C13	C9	176.8(4)
C3	Se1	C4	C11	-42.4(5)
C3	Se1	C4	C13	139.5(5)
C3	C6	C17	C23	1.6(8)
C3	C6	C17	C2	-179.5(6)
C3	C25	C27	C23	1.8(9)
C3	C25	C27	C1	-177.5(6)
C4	Se1	C3	C6	-37.7(5)
C4	Se1	C3	C25	146.8(5)
C4	C11	C22	C15	1.5(9)
C4	C11	C22	C7	179.8(6)
C6	C3	C25	C27	-1.0(9)
C6	C17	C23	C27	-0.9(8)
C6	C17	C2	F5	-70.2(10)
C6	C17	C2	F26	50.8(10)
C6	C17	C2	F29	162.8(7)
C9	C15	C22	C11	-0.7(9)
C9	C15	C22	C7	-179.0(6)
C11	C4	C13	C9	-1.4(9)
C11	C22	C7	F41	50.0(10)
C11	C22	C7	F44	170.9(8)
C11	C22	C7	F45	-67.0(9)

C13	C4	C11	C22	-0.4(8)
C13	C9	C15	C22	-1.1(9)
C13	C9	C37	F14	-139.9(6)
C13	C9	C37	F28	100.9(8)
C13	C9	C37	F53	-20.8(10)
C15	C9	C13	C4	2.2(9)
C15	C9	C37	F14	41.6(9)
C15	C9	C37	F28	-77.5(8)
C15	C9	C37	F53	160.8(7)
C15	C22	C7	F41	-131.7(7)
C15	C22	C7	F44	-10.8(11)
C15	C22	C7	F45	111.3(9)
C17	C23	C27	C25	-0.8(8)
C17	C23	C27	C1	178.5(6)
C23	C17	C2	F5	108.7(10)
C23	C17	C2	F26	-130.3(7)
C23	C17	C2	F29	-18.3(11)
C23	C27	C1	F1	-38.3(12)
C23	C27	C1	F52	-156.7(9)
C23	C27	C1	F58	83.9(13)
C25	C3	C6	C17	-0.6(8)
C25	C27	C1	F1	141.0(9)
C25	C27	C1	F52	22.6(12)
C25	C27	C1	F58	-96.8(13)
C37	C9	C13	C4	-176.3(6)
C37	C9	C15	C22	177.4(6)
C2	C17	C23	C27	-179.7(6)

Table S7 Hydrogen Atom Coordinates ($Å×10^4$) and Isotropic Displacement Parameters ($Å^2×10^3$) for Bis(3,5–bis(triflouromethyl)phenyl)selane.

Atom	x	y	z	U(eq)
H6	6617	985	2311	43
H11	5068	1917	4177	43
H13	6993	5857	3594	43
H15	8739	5322	6671	45
H23	4015	-3462	184	43

| H25 | 1924 | 262 | 697 | 51 |